Development and Testing of a Fairing for a Wind Turbine Tower

---

A Thesis

Presented to

the faculty of the School of Engineering and Applied Science

University of Virginia

---

in partial fulfillment

of the requirements for the degree

Master of Science

---

by

Kyle G. O'Connor

May 2014

APPROVAL SHEET

The Thesis

is submitted in partial fulfillment of the requirements for the degree of

Master of Science

Kyle G. O'Connor

Author

The thesis has been read and approved by the examining committee:

Eric Loth

Advisor

Gabriel Laufer

Haibo Dong

Michael Selig

Accepted for the School of Engineering and Applied Science:

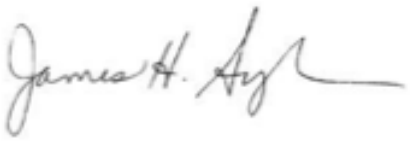

Dean, School of Engineering and Applied Science

May 2014

Acknowledgements

I would like to thank my advisor, Dr. Eric Loth, for his knowledge, guidance, and motivation throughout my graduate studies. I have learnt a tremendous amount from him during our time together. I would also like to thank the other members of Dr. Loth's research group for all of the help they provided me. I would like to thank Dr. Michael Selig for his continued support throughout this project. I would like to thank the sponsors at the National Renewable Energy Lab (NREL) and Dominion Power for funding this project. Finally, I want to thank all of my family and friends for all of the support they have provided me. I would not be where I am today without them.

Contents

List of Figures

List of Tables

Nomenclature

Symbols

c	chord length
C	centrifugal force
C_d	2-D drag coefficient based on chord
$C_{d,D}$	2-D drag coefficient based on tower diameter
$C_{d,t}$	2-D drag coefficient based on maximum thickness
C_l	2-D lift coefficient
$C_{l\alpha}$	slope of the 2-D lift curve
C_m	2-D moment coefficient about the inscribed cylinder center
$C_{m\alpha}$	change in the 2-D moment coefficient with respect to angle of attack
$C_{m,c/4}$	2-D moment coefficient about the quarter chord
C_p	pressure coefficient
D	tower/inscribed cylinder diameter
E	modulus of elasticity
F	total force on the blade
F_d	2-D drag force per unit length
F_Q	torque-wise force

Fr	Froude number
g	gravitational acceleration
G	gravitational force
h	test section height
I	area moment of inertia
J	blade flapping inertia
L	lift force on the blade
Lo	Lock number
m	mass
M	Mach number
p	pressure
r	radial distance from hub
R	rotor radius
Re	Reynolds number based on chord length
Re_D	Reynolds number based on inscribed cylinder diameter
t	airfoil thickness
T	thrust force
u	flow velocity in the x-direction
v	flow velocity in the y-direction
V	total velocity
x	streamline distance along the airfoil chord line from the leading edge
x_D	x location of tower center
x_t	x location of airfoil maximum thickness

x_{TE} x location of trailing edge

X horizontal distance from the left edge of the interrogation window

y normal distance from the chord line

Y vertical distance from the top edge of the interrogation window

α angle of attack

α_b blade angle of attack

α_n harmonic constant

β load-path angle

Λ turbulence scale parameter

λ tip-speed ratio

η length scaling factor

ω natural frequency

ϖ non-dimensional natural frequency

Ω rotor angular speed

φ azimuthal blade angle

ρ density

σ standard deviation; tunnel correction parameter

σ_T turbulence standard deviation

θ_e maximum extreme direction change angle

Subscripts

0	no wake condition
∞	freestream property
c	corrected value
air	property of air
blade	property of the blade
cut-in	cut-in condition
cut-out	cut-out condition
flap	flapping dynamics
fluid	property of the surrounding fluid
hub	property at the wind turbine hub
m	model-scale
p	physical-scale (full-scale)
rated	rated power conditions
rel	relative to the moving blade
u	uncorrected value

Chapter 1

Introduction

The average rated power of wind turbines is growing yearly. As the size of the average wind turbine increases, new designs are needed to handle the increased loads, and some of these designs may require a downwind configuration. Such a configuration requires the wind turbine blades to pass through the turbulent wake of the tower, and this can lead to blade fatigue and, eventually, blade failure. Implementing an aerodynamic fairing around the tower can substantially reduce the effects of the wake on the blades. Ideally, the fairing will meet four objectives: 1) low drag, 2) a short trailing edge relative to the tower center, 3) a moment that results in self-alignment about the tower center, and 4) no large adverse pressure gradients. The prospective fairing designs were analyzed computationally using XFOIL. The computational software was unable to accurately predict flow separation at high Reynolds numbers, so experiments were conducted in a water channel to analyze two airfoils of interest. Flow visualization was used to explore the ability of the airfoils to delay flow separation and particle image velocimetry (PIV) was used to analyze the wake of the airfoils at several angles of attack. Restrictions to the flow speed and model sizes prevented the experimental Reynolds number from being matched with the full-scale Reynolds number. To properly determine the best fairing design, experiments must be conducted at a higher Reynolds number.

Chapter 2

Fairing Design

2.1 Introduction

2.1.1 Motivation

The average wind turbine rated power has increased twenty-fold since 1985 with present large-scale systems greater than 5 MW. Future extreme-scale systems with power levels of 20 MW will have rotor diameters on the order of 240 m. These future "extreme-scale" (10+ MW) systems will be difficult to construct using conventional rotor designs due to the combination of the blade stiffness constraints and increases in blade mass. The rotor cost is approximately linearly proportional to the mass, and the rotor accounts for a significant amount of the total system cost, with many other turbine components increasing in scale and cost as the rotor mass increases. Thus, new concepts in turbine blade design are needed to decrease the mass and increase the cost effectiveness of extreme-scale wind turbines.

Conventional upwind turbine configurations, like the one shown in Fig. 2.1a, typically employ blades with fiberglass shells to carry the structural and aerodynamic loads with small aeroelastic deflection to avoid tower strikes and structural fatigue. The blade stiffness needed to avoid tower strikes and fatigue leads to the blade mass problems discussed above. This stiffness constraint can be relaxed if a downwind morphing concept is employed to reduce the blade mass, which leads to a reduction in cost. The potential to reduce the cost suggests that new large

designs are more likely to have a downwind rotor. A segmented ultralight morphing rotor (SUMR) design was proposed by Loth *et al.*[1] to allow for the manufacture of extreme-scale turbines. A conceptual image of the SUMR design is shown in Fig. 2.1b. In this design, the rotor can begin to morph as the wind speeds increase and then fully-align with the resultant forces at higher wind speeds. The vast majority of stress-inducing cantilever loads on a conventional upwind rotor are due to downwind moments. The forces can combine to induce significant cantilever loads in the downwind direction for a conventional blade. However, if the forces are aligned along the blade, the structural loads are reduced to primarily acting in tension, which drastically reduces the stresses on the blades. This aligning is especially important for extreme-scale systems for which the downwind cantilever forces and gravity stresses rapidly increase blade masses. The downstream angle needed for alignment increases with turbine rated power, making the morphing concept more attractive, especially for 10 MW and higher systems.[2] Initial tests showed that this design may allow for a substantial reduction in blade mass compared to a conventional blade.[3] Other examples of proposed downwind rotors include studies by Hand *et al.*[4] and Rasmussen *et al.*[5]

The most common concern about using a downwind rotor is the effect of the tower wake on the downstream blades. Zahle *et al.*[6] conducted a three-dimensional Navier-Stokes simulation to model the interaction between a wind turbine tower and a downwind rotor blade. They discovered that when the blades were subjected to the velocity deficit in the tower wake they underwent a sudden deloading and subsequent reloading of forces. The sudden change in the aerodynamic loading on the blade can lead to flutter. If the blade experiences a slight flutter every revolution, the effects can be compounded over the life span of the blade, resulting in significant blade fatigue and greatly increasing the chance for blade failure. However, employing

an aerodynamically faired tower, like the one shown in Fig. 2.1c, can mitigate the negative effects that the tower has on the turbine blades. Such a fairing can have a substantial impact because the drag (and turbulent wake) of an airfoil is many times less than that of a cylinder. The shroud can also be allowed to rotate freely about the fixed tower, as shown in Fig. 2.2a, so that it will ideally always be aligned with the wind direction.

One drawback to using a tower shroud with a downwind turbine is that the turbine rotor must be moved further downstream to accommodate for the length of the shroud, as seen in Fig. 2.2b. This increases the downwind cantilever loads that the tower would have to be able to support. In a conventional, upwind configuration the moment caused by gravity acting on the rotor is counteracted by the moment caused by the thrust force of the blades. In a downwind configuration, these two moments compound each other. One possible solution for this problem is to include support cables that can handle the increased cantilever loads, but fixed support cables may limit the range of motion of the wind turbine. Another possible solution is to include a counterweight on the nacelle that would be able to counteract the cantilever loads without limiting the range of motion of the wind turbine.

2.1.2 Previous Studies

One possible solution for mitigating the impact that the tower wake has on the turbine blades is to employ active load control on the blades. Researchers at the University of California, Davis[7-8] have looked into using a microtab-based load control system that is able to account for a 12% change in the freestream velocity. Unfortunately, the blade passage time is so brief that the microtab control system would have to have minimal lag response to be effective.

Many techniques have been implemented in an attempt to reduce the drag of a cylinder. Lee *et al.*[9] installed a small control rod upstream of the cylinder, Mashud *et al.*[10] attached circular rings around the cylinder, and Sosa *et al.*[11] used three-electrode plasma actuators. All three of these techniques resulted in a drag reduction of approximately 25%. Hwang and Yang[12] were able to achieve greater success in reducing the cylinder drag by nearly 40% by installing one splitter plate upstream of the cylinder and another in the cylinder wake. Finally, Triyogi *et al.*[13] were able to reduce the drag of a cylinder by nearly 50% by installing an I-type bluff body upstream of the cylinder. While these flow control methods did reduce the cylinder drag, they could not compare to the more than 90% drag reduction of placing an aerodynamically faired shroud around the cylindrical tower, like the one shown in Fig. 2.3, where the surface coordinates (x and y) are normalized by the fairing chord (c). Such a shroud would significantly reduce the effects of the tower wake on the rotor blades. Note that Fig. 2.3 identifies the normalized values of tower diameter (D) and chord-wise centroid location (x_D) as well as the airfoil maximum thickness (t) and the associated chord-wise location (x_t).

There have been airfoils designed specifically for use as fairings to minimize drag. Some of the most effective of these airfoils are the Eppler strut series, particularly the Eppler 862 (E862) and Eppler 863 (E863) airfoils[14]. These airfoils are great for minimizing drag, but they were not designed to be self-aligning or to resist separation at non-zero angles of attack, both of which are important for the tower shroud. The Eppler strut airfoils were also designed to operate at low Reynolds numbers so they may not perform as well at the higher Reynolds numbers that an extreme-scale wind turbine experiences. New designs need to be created with all of these considerations taken into account, and the performance of the new designs can then be compared to the Eppler strut airfoils to determine the optimal shroud geometry.

There have not been many experiments done to test how much the wake unsteadiness of a wind turbine can be reduced by using an aerodynamically faired tower, most likely due to the fact that conventional turbines use an upwind design where the tower has little influence on the flow that the rotor sees. During their unsteady aerodynamics testing, Hand *et al.*[4] did take wake measurements for NREL while using a symmetric airfoil-shaped shroud (0.46 m thickness, 0.89 m chord) in a downwind turbine configuration, as shown in Fig. 2.4. Unfortunately the test results have not been released.

A study at the Masdar Institute of Science and Technology[15] simulated the interaction between the tower and rotor for a downwind design. The simulation was run using both a NACA0012 airfoil cross-section and a circular cross-section. The airfoil and circular cross-sections resulted in 5% and 57% reductions in the lift forces on the rotor blade, respectively. The researchers observed that the airfoil shaped tower produced a confined wake compared to the cylindrical towers, and had the least overall impact on rotor instability. However, it should be noted that the aerodynamically shaped tower used in this study had a smaller thickness than the cylindrical tower and would not provide the same structural support.

While there have been many studies on techniques for reducing the drag of a cylinder, and several studies have considered the impact of an aerodynamically faired wind turbine tower, nobody has investigated the ideal fairing geometry for a downwind wind turbine tower. Before the ideal design can be chosen, the design requirements must be determined.

2.1.3 Objectives

The primary objective of this study is to develop an aerodynamic shroud for a wind turbine tower that will reduce the effects that the tower wake has on a downwind rotor. This objective is

accomplished by meeting several constraints. Firstly, the shroud needs to be designed to minimize the velocity deficit in the tower wake, which is accomplished by minimizing the tower drag. Reducing this velocity deficit reduces the dynamic unloading and loading of rotor blades as they pass through the wake, thereby reducing flutter that can lead to blade fatigue and failure. Secondly, it is important that the aerodynamic forces on the shroud when at an angle of attack to the wind result in a counter-acting moment about the tower, as this can ensure that the fairing will self-align (though a fairing yaw motor may be needed to accelerate the process in the presence of rapid gusts). Thirdly, the shroud should be reasonably robust (in terms of preventing flow separation) to significant angles of attack. Flow separation of the shroud can lead to a large increase in both the drag and wake turbulence of the tower that would negatively impact the turbine rotor. The distance between the inscribed cylinder center and its trailing edge should be minimized while still meeting the other objectives because this rotor plane must be extended (and cantilevered from the tower) beyond this distance. In summary, the aerodynamic shroud should ideally have: 1) a minimum drag for a given thickness and wind speed to reduce wake effects, 2) a self-correcting moment about the tower center when at finite wind angles of attack to allow self-alignment, 3) significant robustness to prevent flow separation at significant angles of attack, and 4) should have a small chord for a given inscribed diameter, i.e. a small chord-to-diameter ratio. This study is the first investigation of fairing geometries in terms of these four criteria and the first to design a fairing specifically for wind turbine towers.

2.2 Methods

2.2.1 Aerodynamic Parameters

The conventional chord-based drag coefficient for an airfoil is define in terms of the drag force per unit spanwise-length (F_d), the free stream density and velocity (ρ and V) and the airfoil chord length (c) as:

$$C_d \equiv \frac{F_d}{\frac{1}{2}\rho V^2 c} \tag{2.1}$$

To consistently compare the drag of airfoils that may have different chord lengths but surround a tower of fixed diameter, a tower-based drag coefficient is herein defined based on the diameter of the inscribed cylinder (D), as

$$C_{d,D} \equiv \frac{F_d}{\frac{1}{2}\rho V^2 D} \tag{2.2}$$

The conventional chord-based drag coefficient of (2.1) is thus equal to the diameter-based drag coefficient of (2.2) multiplied by the chord-to-diameter ratio (c/D).

The drag coefficient of an airfoil is dependent on the chord-wise Reynolds number defined in terms of the free stream viscosity (m) as

$$Re \equiv \frac{\rho V c}{\mu} \tag{2.3}$$

The Reynolds number (2.3) depends on the chord of the airfoil, therefore it is different for each airfoil. The Reynolds number can be converted to a Reynolds number based on tower diameter, which is constant for each airfoil, *viz*

$$Re_D \equiv \frac{\rho V D}{\mu} \tag{2.4}$$

The Reynolds number based on tower diameter (2.4) is obtained by multiplying the Reynolds number based on chord (2.3) by the tower diameter and dividing by the airfoil chord. For an extreme-scale wind turbine of 15 MW, the diameter-based tower Reynolds number can be estimated using the scaling of the NREL 5 MW reference turbine[16] to yield a tower diameter of 10 m. Combined with a rated wind speed of 12.5 m/s and sea-level normal temperature and pressure for air, this yields $Re_D = 8.3\text{x}10^6$.

One important characteristic for the shroud is that it should self-align with the wind as it changes direction. To check if the shroud is self-aligning, the change in the moment coefficient about the tower center with respect to angle of attack must be calculated, *viz*

$$C_{m\alpha} \equiv \left.\frac{\partial C_m}{\partial \alpha}\right|_{X_D} \tag{2.5}$$

A passively self-aligning shroud, i.e. without a shroud yaw drive, will have a negative $C_{m\alpha}$ value, which means the moment coefficient will be negative at a positive angle of attack and positive at a negative angle of attack. Since only symmetric airfoils are considered in this study and these have zero moment at 0° angle of attack, the $C_{m\alpha}$ herein was based on the moment coefficient at an angle of attack of five degrees, i.e. . $C_{ma}=(C_{m,at5})/5^{\circ}$.

Finally, the airfoil sensitivity to flow separation is based on the combined impact of the boundary layer development and the streamwise pressure gradient. To characterize the distribution of the surface static pressure (p) in non-dimensional terms, one may define the pressure coefficient as

$$C_p = \frac{p - p_\infty}{\frac{1}{2}\rho V^2} \tag{2.6}$$

As angle of attack increases, one may expect the adverse pressure gradients on a surface to increase leading to flow separation. However, predicting the location and condition for

separation is very difficult for a smooth surface at high Reynolds numbers, so the pressure gradient alone cannot be used to determine angle-of-attack robustness.

2.2.2. Computational Method

The prospective shroud geometries were analyzed using XFOIL,[17] an open-source program for the design and analysis of subsonic airfoils. The program was used to determine the drag, moment, and pressure distribution for each design in order to find an airfoil that best meets all of the requirements. Using viscous analysis, XFOIL is able to predict the pressure distribution around an airfoil at a given Reynolds number and angle of attack. It then uses the pressure data to calculate the lift, drag, and moment on the airfoil. XFOIL also enables the user to choose between free and forced transition for laminar to turbulent boundary layer. For forced transition cases, a surface location for transition must be specified. If free transition is used, the program will predict the location based on an e^n transition method. The free transition method is always active, so even if forced transition is used, free transition can occur upstream of the fixed transition location.

While XFOIL has been widely used for the analysis of airfoils in incompressible flow, validation for various Reynolds numbers and transition locations was conducted to assess prediction accuracy with respect to these parameters. The NACA0012 airfoil is useful for validation tests due to the large amount of experimental data available for it. Figure 2.5 shows the drag polar of a NACA0012 at $Re = 9\text{x}10^6$, including experimental data from Abbott and von Doenhoff.[18] For the free transition case XFOIL follows the same trend as the experimental data, though it slightly underpredicts the drag coefficient throughout the domain. The case with transition forced at 30% of the chord length follows the experimental data closely over the entire

domain, indicating that the experimental transition location was near 30% of the chord. The other simulated cases with earlier transition predicted a larger minimum drag than the experimental case, though the data converged to the experimental values at higher lift coefficients, indicating reduced sensitivity to skin friction drag at higher angles of attack, as expected. This result was also observed for other Reynolds numbers. Overall, XFOIL reasonably predicts the drag coefficient, especially if the transition location is known.

To further investigate Reynolds number effects for a thicker airfoil, the drag coefficient and Reynolds number for a NACA0018 airfoil at $\alpha = 0°$ is shown in Fig. 2.6. The airfoil thickness and Reynolds number range were selected based on the experimental data of Blevins[19]. The experimental data indicates a general reduction as Reynolds number increases and the drop-off, at approximately Re = 100,000, occurs due to the transition of the boundary layer from laminar to turbulent flow. For the free transition case, the XFOIL data follows the same trend as the experimental data at the lower Reynolds number (where the boundary layer is mostly laminar) but tends to underpredict drag when the boundary layer is generally turbulent at higher Reynolds numbers. For Reynolds numbers in the range of $3x10^5$-$3x10^6$, the fixed transition simulation at 20% tends to give the best agreement, while a transition of 3% tends to be best for Re=$3x10^6$-10^7. The results are consistent with the transition location moving upstream as the Reynolds number increases, but suggests that the free transition model of XFOIL is not as robust in performance for thick airfoils at high Reynolds numbers, which is the condition associated with tower shrouds for extreme-scale wind turbines. Furthermore, any surface contamination is likely to move the transition location further upstream such that a 3% transition location may be a reasonable approximation for Re>$3x10^6$. However, absent experimental data, the free transition predication may be helpful to provide a lower bound of drag at high Reynolds numbers.

2.3 Shroud Design

2.3.1 Performance Objectives

As mentioned earlier, an aerodynamic shroud ideally meets several requirements in order to be suitable for use with a wind turbine tower. The requirements can be expressed in terms of the defined aerodynamic parameters as:

1) low drag, i.e., minimum $C_{d,D}$
2) short trailing edge relative to tower center i.e., minimum $(x_{TE} - x_D)/D$
3) self-aligning about cylinder center i.e., $C_{m\alpha} < 0$ about x_D
4) avoid strong adverse pressure gradients i.e., avoid large gradients in C_p

The motivation for these requirements can be summarized as follows. Minimizing the drag is directly related to minimizing the effect the wake of the tower has on the rotor blades. A negative $C_{m\alpha}$ will ensure that the shroud will self-align with the wind direction when subjected to a non-zero angle of attack. The shroud should avoid any adverse pressure gradients as these may lead to flow separation that increases the drag and wake turbulence of the tower. Finally, minimizing the distance between the tower center and the trailing edge of the shroud increases the distance between the start of the wake and the rotor plane, and this increased distance will be associated with a reduction in the wake impact on the rotor tip load unsteadiness, thereby reducing the span-wise dynamic cantilever loads to the rotor blade.

2.3.2 Baseline Shroud Geometry

There are many shroud geometries that can lead to a reduction in the tower drag, but some geometries may be more effective than others based on the above requirements. With respect to

the first two requirements of low drag and short chord length, an ideal thickness-to-chord ratio must be determined. Figure 2.7 compares the diameter-based drag coefficients for elliptic airfoils and symmetric NACA airfoils with various ratios of inscribed diameter to chord length (*D/c*). This length-scale ratio is equal to the thickness-to-chord ratio (*t/c*) by assuming the tower circular cross-section is located at the airfoil maximum thickness location (refer to Fig. 2.3). The symmetric NACA airfoil data were calculated using XFOIL at the low Reynolds number of the experimental ellipse data (Re_D=1x10^5) as well as the high Reynolds number associated with a full-scale tower for a 15 MW wind turbine (Re_D=8.3x10^6). Also shown are measurements for cylinders using the various flow control methods as previously discussed. The drag of the symmetric NACA airfoils is significantly lower than the drag of both the elliptical airfoils and the cylinders with flow control. This indicates an aerodynamic airfoil shape is important and can allow the drag to be substantially reduced, e.g. the minimum diameter-based drag coefficient for cylinder flow is about 0.5, while that for an aerodynamic shroud is less than 0.05. Based on these results, a symmetric NACA airfoil was selected for the baseline geometry.

The next step was to determine the approximate thickness-to-chord ratio that would result in the lowest diameter-based drag. XFOIL was used to help determine where the combination of pressure and skin-friction drag is minimized. Figure 2.8 shows the predictions at the full-scale tower Reynolds number, Re_D = 8.3x10^6 for both free and fixed transition at 3% chord and 0° angle of attack. Based on the results of Fig. 2.6, the former can be expected as a lower bound while the latter may be more accurate. The diameter-based drag was minimized at a 33% thickness ratio for the case of fixed transition at 3% chord and at a 38% thickness-to-chord ratio for the free transition case. Larger thickness ratios resulted in increased drag due to pressure-based (profile) drag while lower thickness ratios resulted in increased drag due to viscous-based

(skin friction) drag. However, both cases were not strongly sensitive to changes in thickness ratios between approximately 30% and 40% for this 0° angle of attack condition. In reality the tower shroud may accumulate debris near its leading edge so the resulting surface roughness will most likely cause the boundary layer to transition to turbulent near the leading edge, so the fixed transition case will generally be more physically realistic than the free transition case at these high Reynolds numbers. For this reason, the minimum drag was based on the fixed transition case, yielding a baseline geometry of a NACA0033 airfoil, which has a 33% thickness ratio. The tower is initially assumed to be located at the maximum thickness, which occurs at 30% of the chord, to provide the minimum diameter-based drag.

If one next considers the self-fairing objective, attention must be paid to the pitching moment coefficient. Unfortunately, the NACA0033 has a positive C_{m_α} about the cylinder centroid location based on the XFOIL predictions. As a result, if the flow approaches at a positive angle of attack, the aerodynamic moment will be in the positive angle of attack direction. Therefore, this moment will cause the shroud to rotate to higher angles of attack so that it will become further misaligned, resulting in a large increase in the drag and effects of the tower wake on the downstream turbine blades. As such, this airfoil is statically unstable and not self-aligning about the maximum thickness location. This was expected because the tower center is located at 30% of the chord length, which is aft of the quarter-chord which corresponds to the aerodynamic center for a thin symmetric airfoil. To achieve a negative pitching moment for self-aligning, the tower center will generally have to be in front of the quarter-chord.

2.3.3 Airfoil Designs

In an attempt to create a shroud with minimum drag and a negative C_{m_α} about the tower center, a series of new 33% thick semi-cylinder airfoils were developed with the maximum thickness locations closer to the leading edge of the airfoil. The new airfoils were created by starting from a NACA0028, NACA0030 and NACA0031, all three of which have the maximum thickness located at 30% of chord. The front end of each airfoil was then trimmed off so that the leading edge of the airfoil was a cylinder centered about the maximum thickness location. By making this change, the maximum thickness locations for the airfoils are closer to the leading edge thereby increasing the potential to have a negative C_{m_α} about this location.

While simple in design, these semi-cylinder airfoil geometries (a semi-cylinder up to the maximum thickness and a NACA airfoil for the remainder) resulted in a blunted leading edge and a thickness-to-chord ratio greater than the optimal 33%, both of which can lead to an increase in drag. This problem was remedied by adding a finite thickness "cuff" section to the leading edge semi-cylinder of each airfoil. This extra material reduced the thickness to yield a 33% thickness ratio while also reducing the bluntness. To achieve a 33% thick airfoil, the airfoil that originated from the NACA0031 required a cuff that was 10% of the chord length. The airfoils that originated from the NACA0028 and NACA0030 required cuffs that were 1.15% and 7.1% of their chord lengths respectively. The three resulting cuffed airfoils were named the C28, C30 and C31 where the C stands for 'cuff' and 28-31 indicates the symmetric NACA airfoil that describes the aft portion. The C30u geometry is shown in Fig. 2.9a along with the inscribed cylinder. It can be seen that the maximum thickness (and cylinder centroid) is now located forward of the quarter chord.

The drag and moment coefficients for these "simple-cuff" airfoils were obtained at the full-scale Reynolds number using XFOIL. The results show a tradeoff between the drag and pitching moment. The C31 has the lowest drag of the new airfoils but it also has a slightly positive C_{m_α}. On the other hand, the C28 has the best C_{m_α} but it also has the highest drag. Unfortunately, the maximum thickness merger location of the cuff and aft airfoil section included a discontinuity in curvature, which led to locally large adverse pressure gradients that may lead to separation at significant angles of attack. Therefore, a continuous-curvature design was next investigated to eliminate the curvature discontinuities and to further reduce the drag while also maintaining a negative C_{m_α} value.

The continuous-curvature advanced design was conducted using PROFOIL,[20] which is an inverse design method that allows for the prescription of the desired velocity distribution around the airfoil from which the geometry is determined. The method was applied with and without a slope constraint to modify the above three simple-cuff airfoils, resulting in six new airfoils to go along with the three originals. The new constraint required that the surface geometric slope be zero at the original maximum thickness location (as was the case for the simple cuff airfoils). The airfoils that were created with the constraint are designated with a 'c' in the airfoil name, e.g., C30c, and are referred to as the 'constrained' series. The airfoils that were created without the constraint are designated with a 'u', e.g., C30u, and are referred to as the 'unconstrained' series. The difference between the airfoil series can be seen in Fig. 2.9. Figure 2.9a shows the simple cuff airfoil, while Fig. 2.9b shows an airfoil that was created with the zero-slope constraint, and Fig. 2.9c shows an airfoil that was created without the constraint.

It is important to note that the inscribed cylinder centroid can be moved forward of the maximum thickness location to further improve the pitching moment without changing the

fairing geometry. However, moving the tower centroid further upstream necessitates that it have a smaller diameter to stay inscribed. For a fixed tower diameter, this is equivalent to increasing the maximum thickness and chord length to accommodate this upstream tower location. Generally, this will increase the diameter-based drag (and diameter-based drag coefficient) since now the maximum airfoil thickness will be larger than the cylinder diameter as shown in Fig. 2.3. However, this centroid movement was investigated because some of the airfoils had an undesirable positive pitching moment when the tower is located at the maximum thickness. In general, the cylinder centroid (i.e. tower centroid) location can be moved for each airfoil to find the best balance between the $C_{d,D}$ and $C_{m\alpha}$.

2.4 Results

A total of nine airfoils were examined to determine how they performed with respect to the objectives. These nine airfoils consist of the baseline NACA0033, two Eppler strut airfoils, three 'constrained' airfoils, and three 'unconstrained' airfoils. The basic geometry and zero-lift drag characteristics of these airfoils are given in Table. 2.1. For simplicity, they were all evaluated at a chord-wise Reynolds number which is consistent with the full-scale diameter-based Reynolds number and a chord to thickness ratio of 3:1.

The nine airfoils were analyzed using XFOIL to determine their drag and pitching moment performance. Figure 2.10 shows the drag and moment for each airfoil based on the cylinder centroid location (x_D) for both free and fixed transition cases at 0° angle of attack. The minimum drag for each airfoil occurs when the cylinder centroid is located at the maximum thickness, and this point is marked with a solid symbol for each airfoil. As the cylinder centroid moves closer to the leading edge of the airfoil, $C_{m\alpha}$ decreases. The point where the cylinder centroid is at 20% of

the chord is marked with a hollow symbol for each airfoil. For the free transition case, the E863 had the lowest drag, followed by the E862, C31u and C30u airfoils. All of these airfoils are also able to achieve a negative $C_{m\alpha}$ value without a significant increase in the drag. For the fixed transition case, the difference between the minimum drag for all of the airfoils is greatly reduced. The E863 airfoil still has the lowest minimum drag, but the E862 airfoil has lower drag when the $C_{m\alpha}$ value is negative. None of the other seven airfoils were able to achieve a negative $C_{m\alpha}$ value without a significant increase in the drag.

Table 2.2 gives a comparison of various airfoil properties when the cylinder centroid is at the minimum drag location (i.e. at maximum thickness location) for each airfoil. This data is for fixed transition near the leading edge of the airfoils because it is most indicative of the flow the turbine shroud will experience. At 0°, the E863 airfoil has the lowest drag, but there is only about a 5% difference between the highest and lowest drag airfoils. At 10° the E862 airfoil has the lowest drag, and the differences in the drag of the various airfoils are more pronounced. The C30u and C31u have the highest drag at a 10°. The Eppler strut airfoils have a significantly lower $C_{m\alpha}$ value than the other airfoils, but it is still positive for both. Therefore, the cylinder centroid has to be moved from the maximum thickness for all of the towers in order to achieve a negative $C_{m\alpha}$.

The distance from the cylinder centroid to the trailing edge of the shroud, represented non-dimensionally by $(x_{TE} - x_D)/D$, is dependent on a combination of the chord length of the airfoil and the location of the cylinder centroid along the chord line. One of the objectives is to minimize this distance because it reduces the distance the turbine rotor must be located downstream, which in turn reduces the cantilever loads that the tower must be able to support.

The E863 airfoil has the shortest cylinder centroid to trailing edge distance of all of the airfoils, while the C28c airfoil has the longest cylinder centroid to trailing edge distance.

The final constraint to consider is the avoidance of large adverse pressure gradients. Figure 2.11 shows the pressure distributions at both 0° and 10° angles of attack for the five primary airfoils of interest. At 0° the Eppler strut airfoils have an aggressive pressure curve with a steep adverse pressure gradient near 50% of the chord. This type of pressure distribution most likely contributes to the low drag of the airfoils, but it may also lead to separation depending on the state of the boundary layer properties. The NACA0033 has the smoothest (most benign) pressure gradient, and the unconstrained airfoils fall in between the NACA0033 and Eppler strut pressure distributions. At 10°, the predicted pressure distributions indicate that the flows around the unconstrained airfoils separate around 60% of the chord and the flow around the NACA0033 separates around 80% of the chord. Surprisingly, the flow around the Eppler strut airfoils remains attached despite having the most aggressive pressure distribution. Unfortunately, XFOIL nor any other current computational fluid dynamics tools are adept at predicting separated flow at high Reynolds numbers, so it is difficult to determine separation robustness without experimental studies. Without experimental studies at high Reynolds numbers, it is difficult to determine which airfoil is truly the best design for the wind turbine shroud problem. The E863 has the lowest drag at 0°, while the E862 has the lowest drag at 10°, and would be generally recommended at low Reynolds numbers for which they were specifically designs. However, both Eppler airfoils have a more aggressive pressure distribution than the C30u and C31u airfoils. The latter two airfoils, which have a reasonably small drag and pitching moment coefficients, may also be of interest for use as an aerodynamic shroud.

2.5 Conclusions

The aerodynamic fairing of a wind turbine tower used with a downwind rotor was considered in terms of four design requirements: 1) low drag, 2) a short trailing edge relative to the tower center, 3) a moment that results in self-alignment about the cylinder center, and 4) no large adverse pressure gradients. This study is the first to design a fairing specifically for wind turbine towers based on these four criteria. To address these requirements, several aerodynamic designs were developed and investigated for the tower shroud using XFOIL to describe the aerodynamic performance.

A comparison between the drag of symmetric NACA airfoils and elliptical airfoils showed that the NACA airfoils had the lower drag of the two. Symmetric NACA airfoils with different chord-to-thickness ratios were compared, and it was determined that a three-to-one chord-to-thickness ratio results in the minimum drag for a fixed thickness, so the baseline design was chosen to be a NACA0033 airfoil. Unfortunately, the pitching moment of the NACA0033 at non-zero angles of attack would result in the fairing further misaligning with the wind direction when the tower is located at the maximum thickness (i.e. minimum drag location).

Six new airfoils were created, and they were analyzed along with two Eppler strut airfoils that exhibit low drag behavior and the baseline NACA0033. The nine airfoils were analyzed to find their drag and pitching moment with respect to various cylinder centroid locations. The E863 airfoil had the lowest drag at 0° and had the second best pitching moment. The E863 airfoil also had the shortest distance between the cylinder centroid and the trailing edge. The E862 had the lowest drag at 10° and had the best pitching moment. Both Eppler strut airfoils performed well in terms of drag and pitching moment, but their aggressive pressure distribution may lead to flow separation. Of the other airfoils, the C30u consistently displayed the best performance with

respect to drag and pitching moment when considering both free and fixed transition cases. Unfortunately, no current computational fluid dynamics tools are adept at predicting separated flow at high Reynolds numbers, so it is difficult to determine which design is truly the best for a wind turbine tower fairing. Experimental testing at high Reynolds numbers is suggested to determine which airfoil is the best design for the tower shroud.

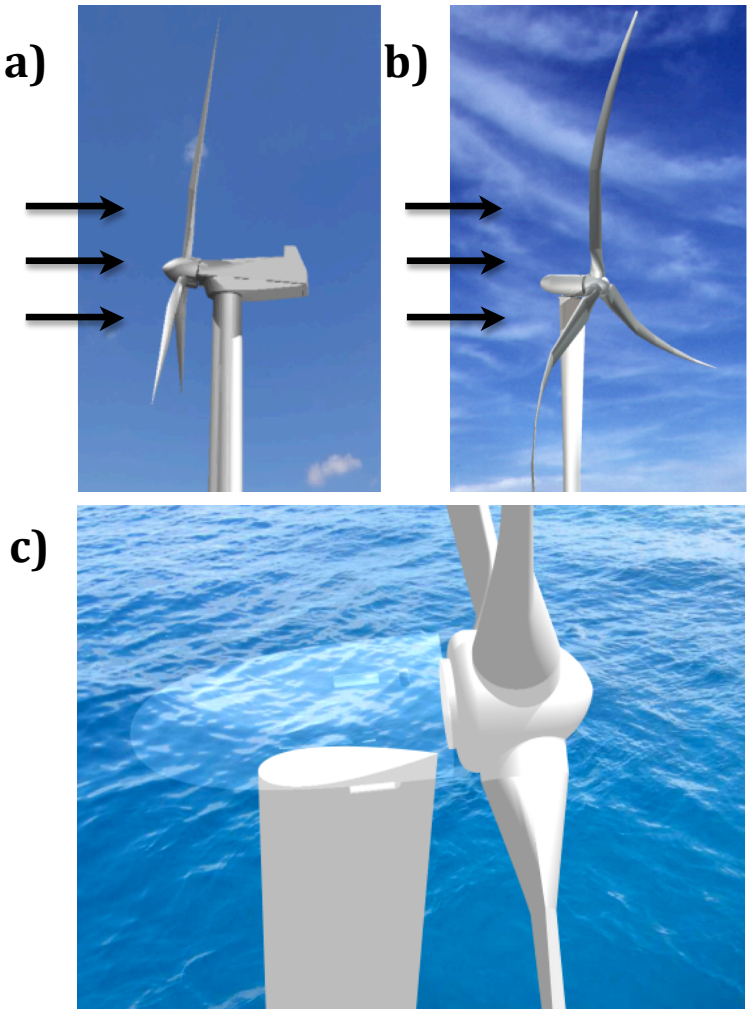

Figure 2.1: Conceptual images of: a) a conventional upwind rotor, b) a downwind morphing rotor, and c) an aerodynamically faired tower for reduced tower wake effects (from Loth et al.[2]).

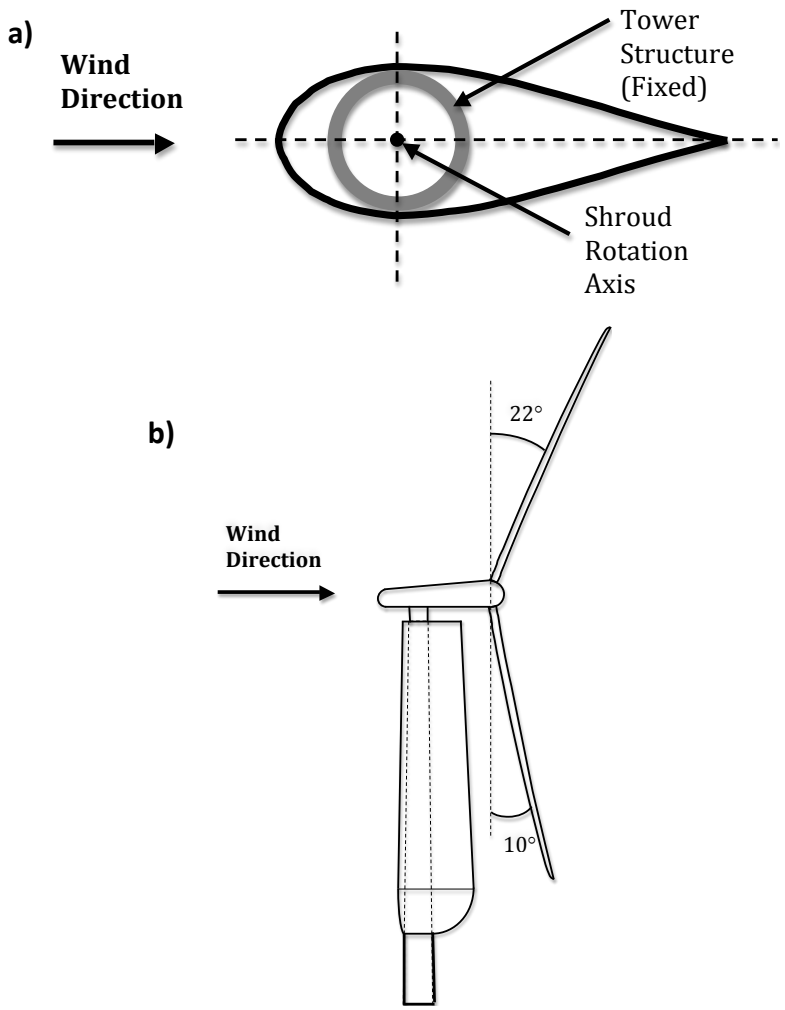

Figure 2.2: Schematic drawings of: a) the tower structure and surrounding shroud and b) the full wind turbine system.

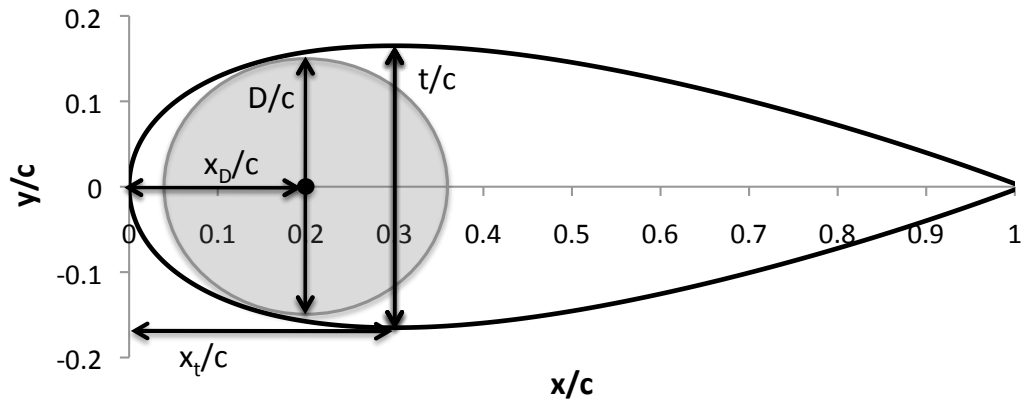

Figure 2.3: Geometry of the NACA0033 and location of tower cylinder.

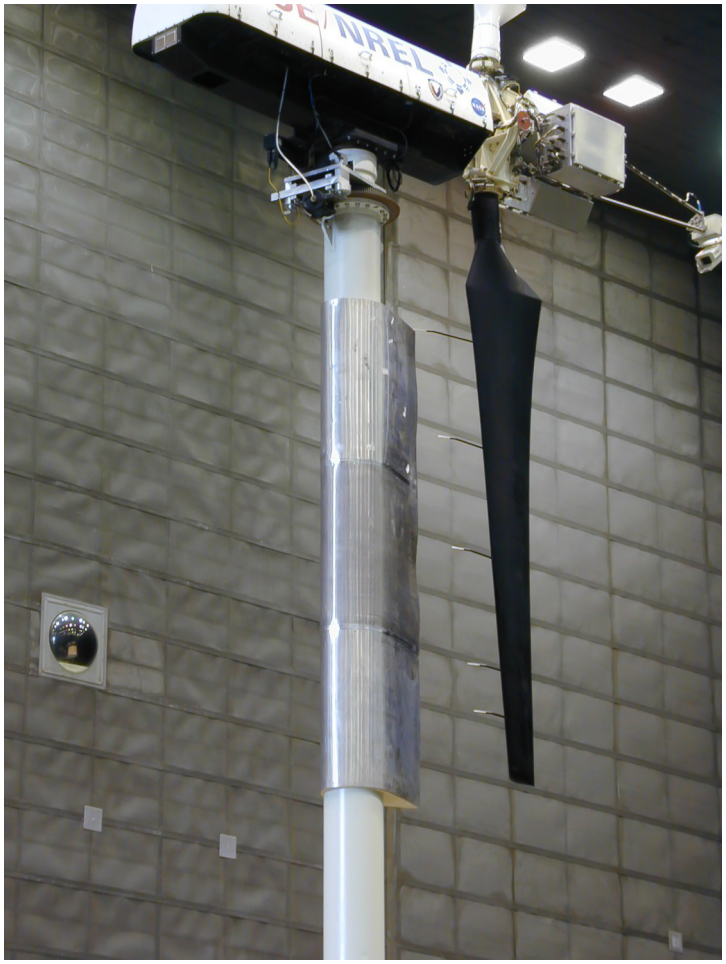

Figure 2.4: Aerodynamic shroud used in NREL unsteady aerodynamics tests (P. Moriarty, personal communication, January 24, 2014).

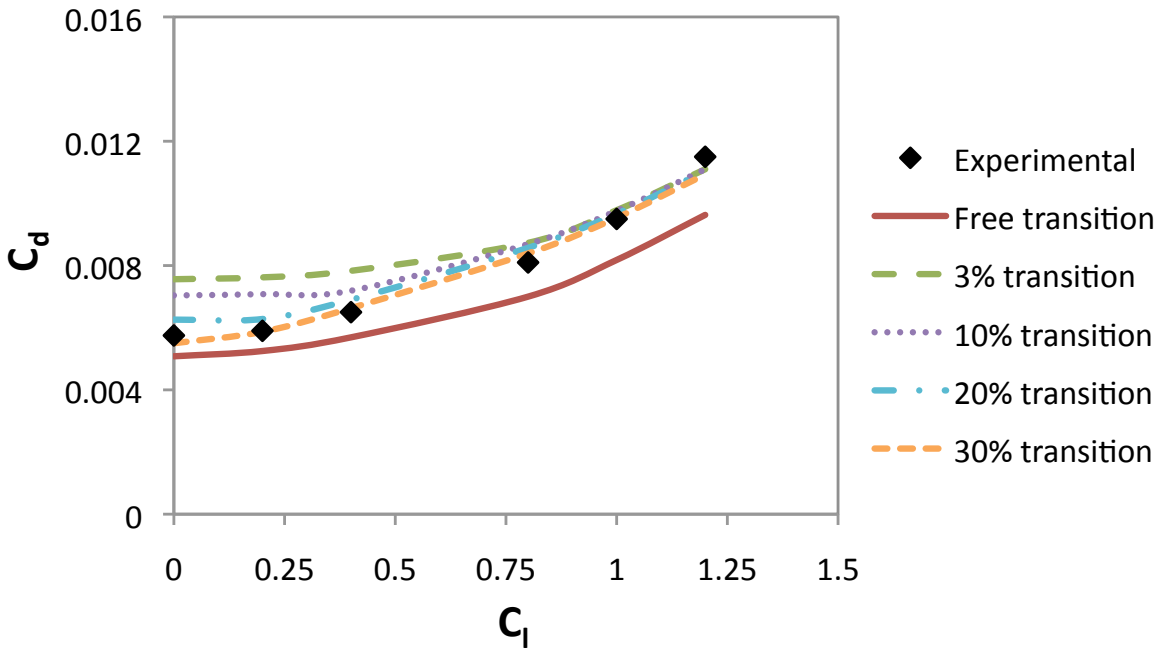

Figure 2.5: Drag polar of a NACA0012 airfoil comparing experimental data and XFOIL predictions for Re=9x10^6 (experimental data from Abbott and von Doenhoff[18]).

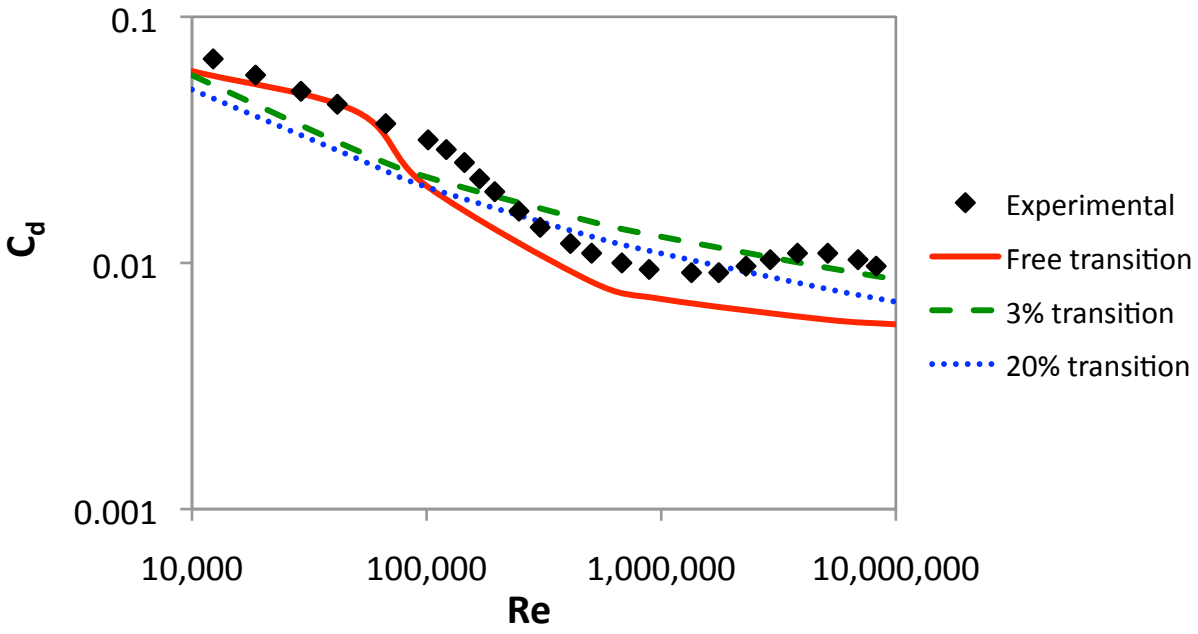

Figure 2.6: Drag as a function of Reynolds number of a NACA0018 airfoil at $\alpha = 0°$ for experimental data and XFOIL predictions (experimental data from Blevins[19]).

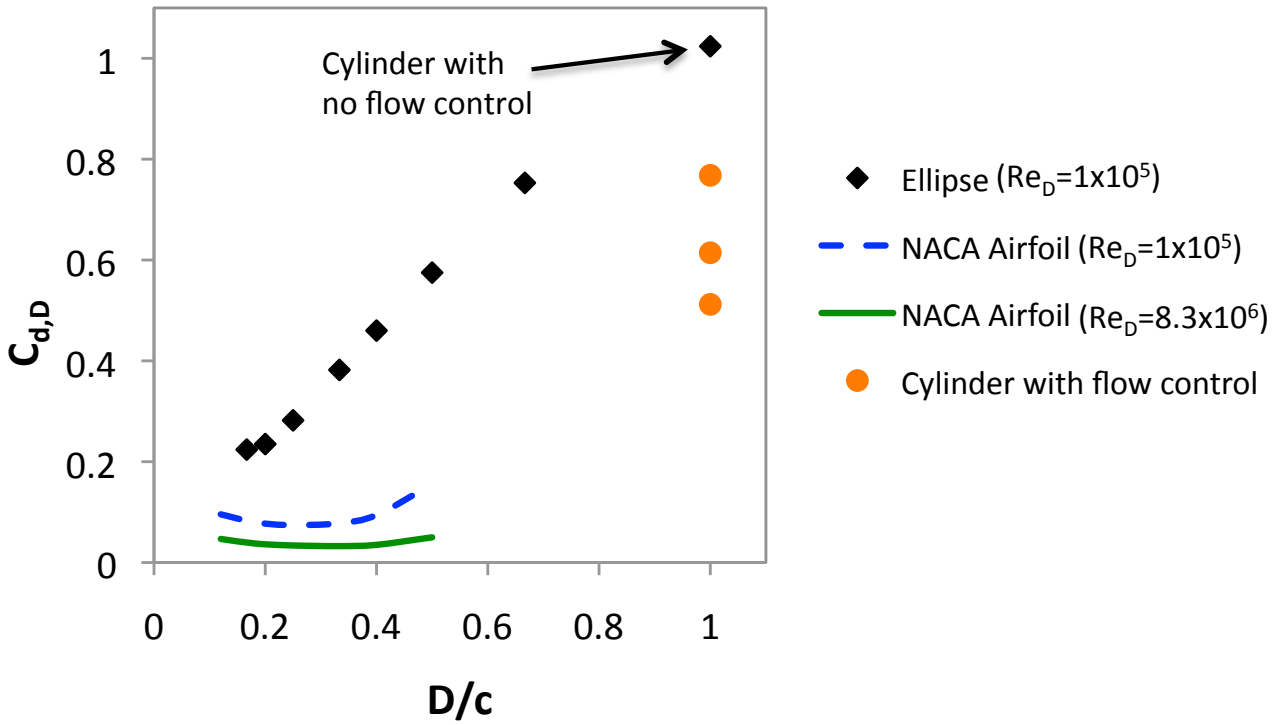

Figure 2.7: Drag coefficient at 0° angle of attack for a cylinder, ellipses, and symmetric NACA airfoils ranging from NACA0012 to NACA0050, where D is the maximum circle diameter that can be inscribed in a given shape (ellipse data from Blevins,[19] and cylinder flow control data from Lee et al.[9], Hwang et al.[12], and Triyogi et al.[13]).

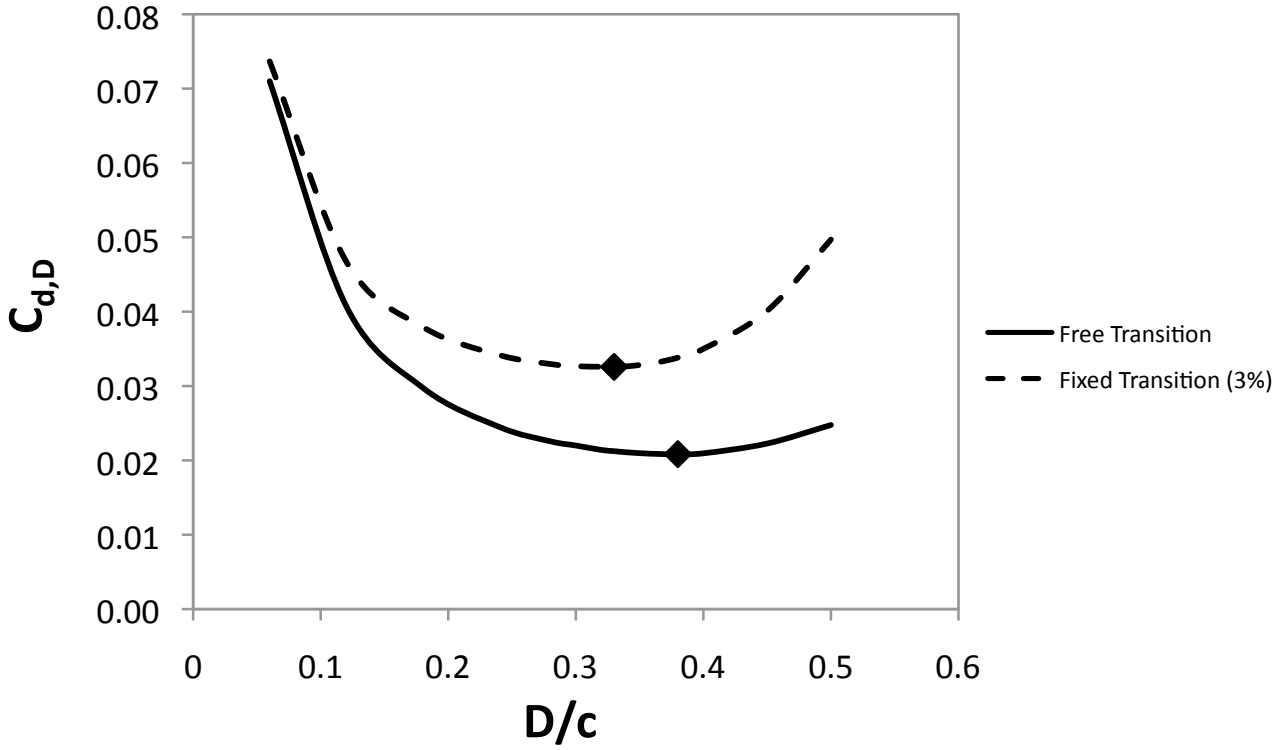

Figure 2.8: Drag coefficient for symmetric NACA airfoils at $Re_D = 8.3x10^6$ for free and fixed transition (markers indicate minimum drag).

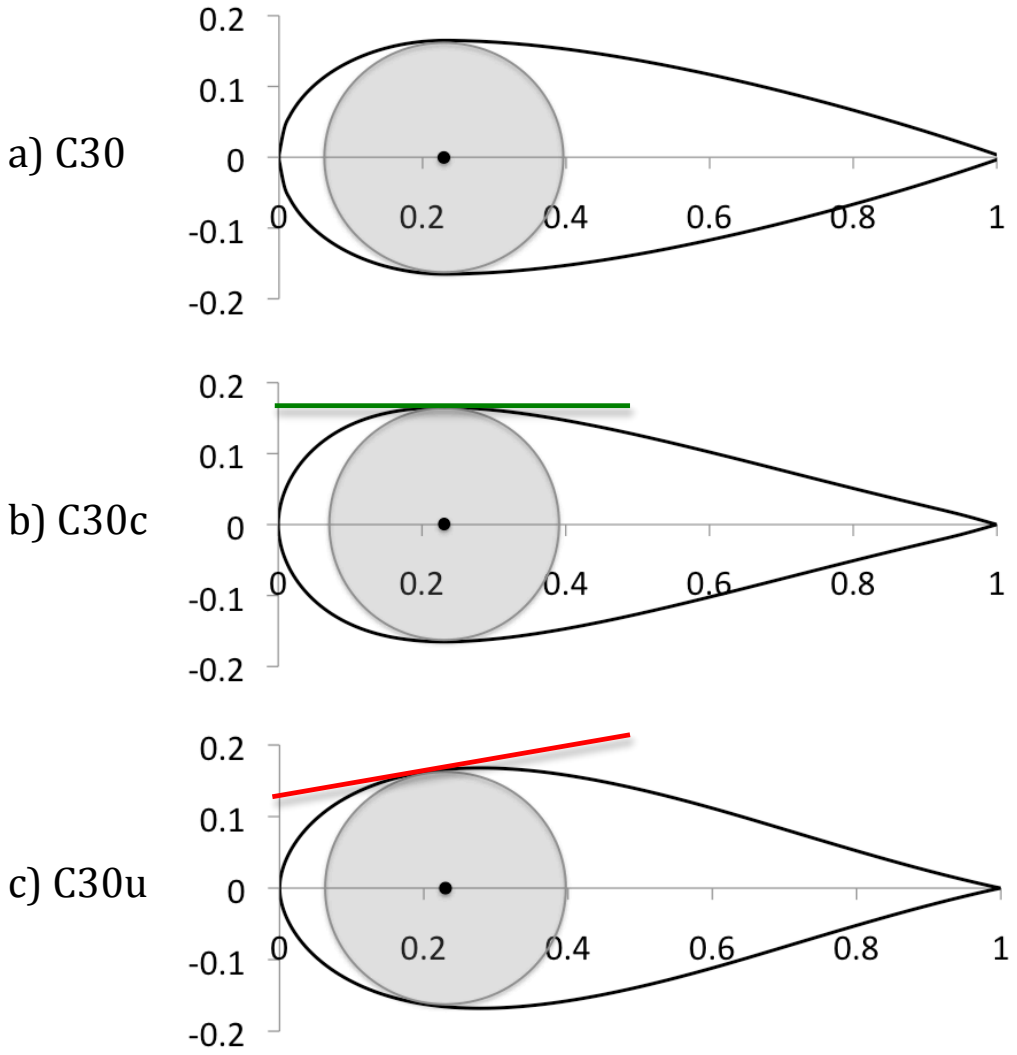

Figure 2.9: Schematic of the a) C30 airfoil, b) modified C30 airfoil with a zero-slope constraint and c) modified C30 airfoil without a zero-slope constraint.

Table 2.1: Constant Airfoil Properties at Re = $25x10^6$

Airfoil	t / c	x_t / c	C_d *at 0° (free trans.)*	C_d *at 0° (fixed 3% trans.)*
NACA0033	0.330	0.301	0.00701	0.01077
C28c	0.331	0.196	0.00795	0.01073
C30c	0.330	0.225	0.00706	0.01042
C31c	0.330	0.253	0.00729	0.01063
C28u	0.355	0.248	0.00748	0.01123
C30u	0.336	0.279	0.00645	0.01059
C31u	0.333	0.284	0.00627	0.01059
E862	0.324	0.285	0.00587	0.01019
E863	0.357	0.285	0.00598	0.01103

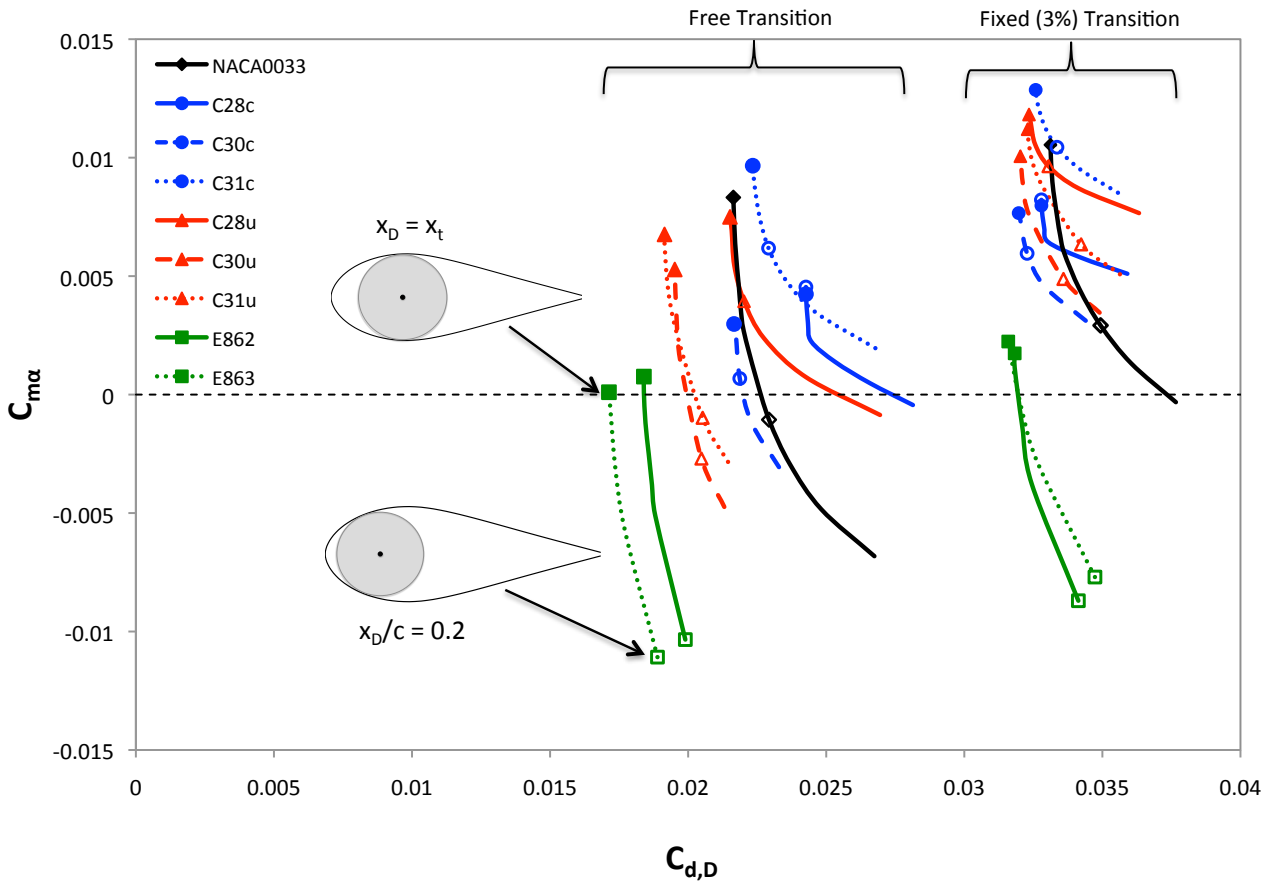

Figure 2.10: Drag coefficient at zero-lift ($\alpha = 0°$) and pitching moment coefficient based on tower location for $Re_D = 8.3x10^6$.

Table 2.2: Airfoil Properties at Minimum Drag Location with Fixed Transition at 3% of the Chord

Airfoil	x_D / c	D / c	$(x_{TE} - x_D)/D$	$C_{d,D}$ *at 0°*	$C_{d,D}$ *at 10°*	$C_{m\alpha}$
NACA0033	0.301	0.324	2.157	0.03312	0.05312	0.01054
C28c	0.196	0.326	2.466	0.03279	0.04656	0.00798
C30c	0.225	0.325	2.385	0.03197	0.05138	0.00766
C31c	0.253	0.325	2.298	0.03258	0.05385	0.01286
C28u	0.248	0.350	2.149	0.03234	0.06003	0.01182
C30u	0.279	0.330	2.185	0.03203	0.06282	0.01006
C31u	0.284	0.327	2.190	0.03229	0.06471	0.01120
E862	0.285	0.318	2.248	0.03182	0.04525	0.00174
E863	0.285	0.352	2.031	0.03159	0.05906	0.00224

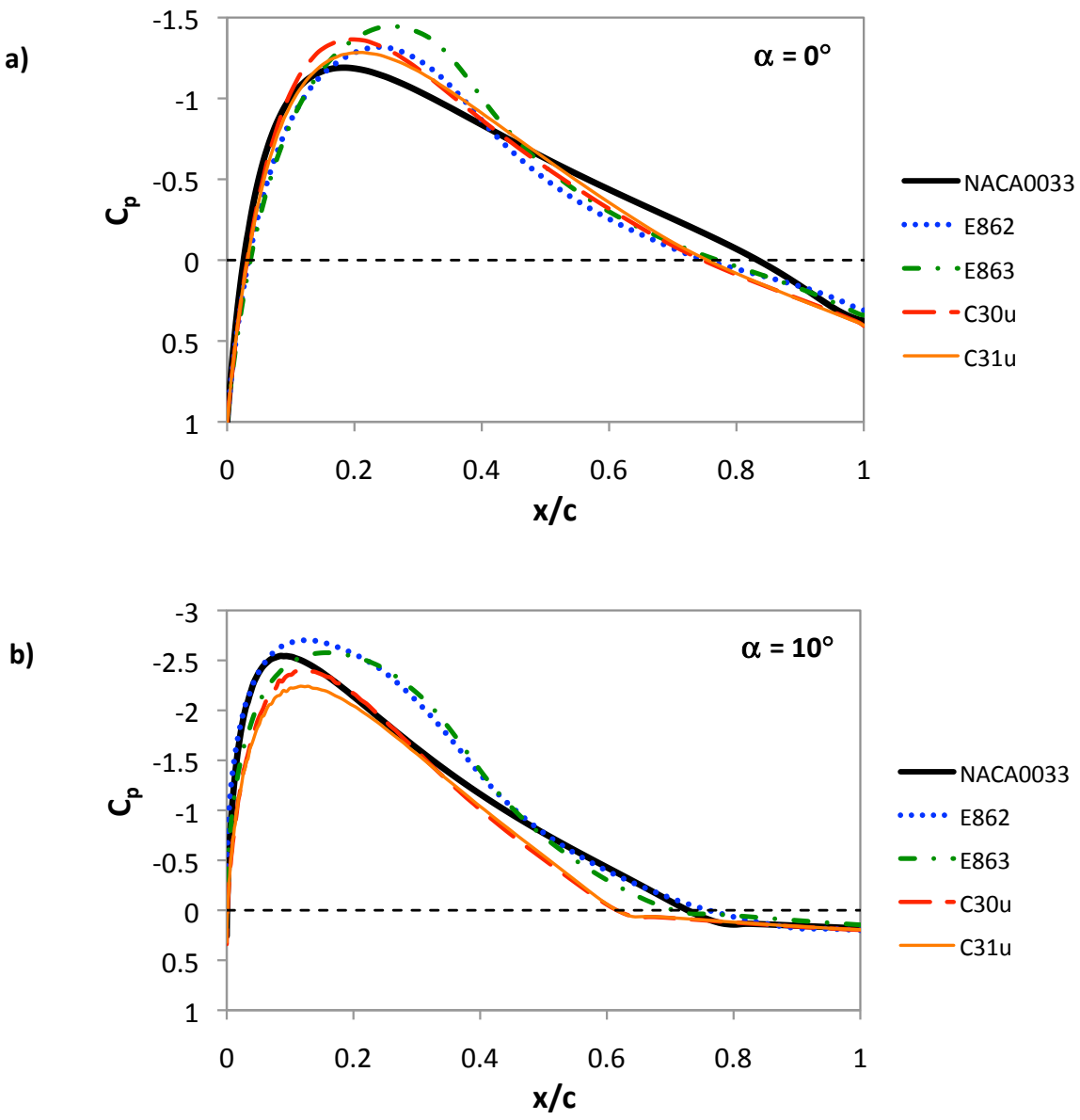

Figure 2.11: Pressure distribution over the upper surface for select airfoils with fixed transition at 3% of the chord and Re = 25x10^6 at: a) 0°angle of attack and b) 10° angle of attack.

Chapter 3

Water Channel Experiments

3.1 Introduction

3.1.1 Motivation for Experiments

In chapter two, several airfoils were analyzed using XFOIL to determine the best geometry for a tower fairing for a downwind wind turbine configuration. These results were helpful in narrowing down the potential fairing geometries, but further analysis is necessary to determine the best design. Experiments were conducted to compare the airfoils' abilities to delay flow separation and to analyze the wake downstream of the airfoils, both areas in which XFOIL is not particularly well suited. The experiments were conducted in a water channel located at the University of Virginia, and flow visualization and particle image velocimetry (PIV) were the experimental methods that were used.

3.1.2 Flow Visualization

Flow visualization is a simple experimental technique where a visible substance is introduced into the flow so that the flow dynamics can be observed. Flow visualization is generally more useful for acquiring qualitative results than quantitative results. The tracer substance must be able to follow the flow, and for this reason dyes are most commonly used in water and smoke is most commonly used in air.[21] Solid or gaseous tracers as well as floating agents may also be used

for flow visualization in water, but liquid tracers, such as dyes, are best suited to follow the flow.[22] Using flow visualization to observe aerodynamic flow phenomena in a water tunnel has the advantage that at the same Reynolds number the flow can be observed at a slower speed.[23]

3.1.3 Particle Image Velocimetry

PIV is a non-intrusive method for measuring instantaneous velocities in a flow field. Unlike other techniques that require probes in the flow to take measurements, PIV does not disrupt the flow field it is measuring. For PIV, the flow is seeded with small tracer particles that follow the flow exactly. A laser beam passes through a series of lenses to produce a laser sheet, and the laser sheet is used to illuminate the particles in the area of interest. The laser is synchronized with a camera, and two pulses from two aligned lasers are fired in quick succession to capture two images of the particles with a known time between them. The PIV software uses the two images to determine the distance each illuminated particle traveled in the given time and calculates the particle velocity. Each image is broken up into individual interrogation spots, and all of the particle velocities in an interrogation spot are averaged into a single velocity vector. The velocity vectors from all of the interrogation windows are combined to create an instantaneous velocity field. A large number of these instantaneous fields can be averaged to find the average flow field.

3.2 Experimental Methods

3.2.1 Experimental Setup

In the computational analysis The Eppler strut airfoils, particularly the E863, exhibited the best performance. These airfoils also displayed a very aggressive pressure distribution that may

lead to early separation, a parameter that current fluid dynamic tools are not adept at predicting. The C30u design had the best performance of the remaining airfoils that were considered. Models of the E863 and the C30u airfoils were created for the experiments. A schematic of the airfoil geometries are shown in Fig. 3.1. The airfoil models were made of ABS plastic using a 3-D printer. The Reynolds number for the experiments is significantly lower than the full-scale Reynolds number, so the airfoil models had to be made as large as possible, to maximize the Reynolds number, without introducing significant blockage effects. This resulted in a maximum airfoil thickness of 67 mm. The models were sanded and painted with a polyurethane coating to give them a smooth surface. A cylinder with a diameter equal to the thickness of the airfoil models was also used as a baseline to compare the airfoils' performance.

The experiments were conducted in a water channel located at the University of Virginia. The water channel has a maximum flow velocity of 1 m/s. Ideally the maximum flow velocity would be used to maximize the Reynolds number, but the higher flow velocities introduced unwanted free surface effects, as seen in Fig. 3.2a. These effects are even greater at larger angles of attack, and for a nose-up orientation, the curvature of the free surface can help keep the boundary layer attached when it would normally separate. To help reduce the effects of the free surface on the flow, the angles of attack herein are defined as positive for a nose-down orientation. Since all of the airfoils in the experiments are symmetric, the performance is the same at positive and negative angles of attack. It was determined that a flow velocity of 0.5 m/s was the maximum velocity that didn't introduce significant free surface effects, as seen in Fig. 3.2b.

The Reynolds number based on the inscribed diameter for the models turned out to be $Re_D = 3.35 \times 10^4$, which is two orders of magnitude lower than the full-scale Reynolds number of $Re_D =$

8.33×10^6. To help compensate for the disparity in the Reynolds number, a trip strip was placed near the leading edge of the models to trip the laminar boundary layer to the turbulent regime. While the difference in the Reynolds number means that the experiments will not fully predict the flow of the full-scale system, the experiments ate still useful for comparing the two airfoils to determine which is the best design.

The experiments were conducted at three angles of attack: 0°, 10°, and 20°. According to the International Electrotechnical Commission (IEC) standards for wind turbines,[24] a wind turbine must be designed to handle an extreme direction change (EDC) of angle θ_e with the change of direction occurring over six seconds. The angle is calculated by

$$\theta_e = 4\tan^{-1}\left(\frac{\sigma_T}{V_{hub}\left(1+0.1\left(\frac{2R}{\Lambda}\right)\right)}\right) \tag{3.1}$$

where σ_T is the turbulent standard deviation, V_{hub} is the wind speed at the hub height, R is the rotor radius, and Λ is the turbulence scale parameter. For the full-scale wind turbine, this angle was calculated to be 28°. Since the tower fairing will self align with the wind direction, the maximum angle the fairing will experience will be less than the EDC angle.

The influence of the water channel walls must be taken under consideration. The calculations for the tunnel corrections were taken from Selig and McGranahan.[25] The corrected angle of attack is calculated, *viz*

$$\alpha_c = \alpha + \frac{57.3\sigma}{2\pi}\left(C_{l,u} + 4C_{m,c/4,u}\right) \tag{3.2}$$

where α_c is the corrected angle of attack, α is the physical angle of attack, $C_{l,u}$ is the uncorrected lift coefficient, $C_{m,c/4,u}$ is the uncorrected moment coefficient about the quarter chord, and σ is the tunnel correction parameter calculated by

$$\sigma = \frac{\pi^2}{48}\left(\frac{c}{h}\right)^2 \tag{3.3}$$

where c is the airfoil chord length and h is the height of the test section. For the 0° angle there is no correction that needs to be made because the lift and moment coefficients are both zero. For the 10° cases, the corrected angle was calculated to be 10.30° for the C30u, and 10.08° for the E863. For the 20° cases, the corrected angle was calculated to be 20.17° for the C30u, and 20.15° for the E863. These angle corrections are minimal, and should not have a significant effect on the results.

3.2.2 Flow Visualization Setup

The flow visualization experiments were conducted using direct injection of a water-based dye. The dye system uses pressure regulation to control the dye flow rate. The dye was injected into the flow through a tube that passed through the inside of the airfoil to a hole in the bottom surface of the airfoil near the leading edge. Passing the tube through the airfoil instead of placing the tube directly in the flow ensures that the flow is not disturbed. The dye was injected at a low velocity to ensure that the dye accurately follows the flow. The flow visualization experiments were used primarily to look for flow separation at various angles of attack.

3.2.3 Particle Image Velocimetry Setup

PIV measurements were taken for seven cases: a cylinder, the C30u at 0°, 10°, and 20°, and the E863 at 0°, 10°, and 20°. A schematic of the PIV setup is shown in Fig. 3.3. The flow was seeded using hollow glass spheres with diameters of 8-12 μm. For the C30u and E863 cases, the laser sheet was positioned behind the airfoil trailing edge to capture the wake region. For the cylinder case, the laser sheet was positioned such that the distance from the cylinder to the interrogation window is the same as the distance from the maximum thickness of the airfoils to the interrogation window.

The PIV experiments were conducted using the equipment specified in Table. 3.1. The time step for each case was chosen to maximize the percentage of good vectors collected, which typically occurs when the particles travel approximately 1/4 of the interrogation spot size. The time step varied between 200 and 600 μs depending on the test case. The images were processed with the Insight 4G software from TSI. The processing was done using a Nyquist grid with an interrogation spot size of 64x64 pixels. Post-processing was used to eliminate any vectors that were outside of the velocity tolerance of the local median velocity. The PIV setup was able to produce approximately 80% good vectors. The majority of the error occurred around the edges where particles can leave and enter the interrogation window between the two images. Five hundred image pairs were captured for each case to calculate the average flow field. Uzol and Camci[26] conducted a study on the effect of sample size on the averaged PIV measurements. For the flow field that was studied, increasing the sample size beyond five hundred image pairs had little effect on the accuracy of the average flow field.

The PIV results were used to display the instantaneous velocity, average velocity, and average turbulence fields of the model wakes. MATLAB was used to plot the *u*- and *v*-velocity

profiles at fixed X locations of one and two diameters downstream of the left edge of the interrogation window.

The main purpose of this study is to determine the fairing geometry that will result in the smallest perturbation of the aerodynamic forces on the turbine blade as it passes through the wake. The force perturbation was defined as the change in the forces on the blade as it passes through the wake normalized by the unperturbed aerodynamic forces. If it is assumed that the lift force on the blade is much greater than the drag force (which is reasonable for a wind turbine blade), the force perturbation can be simplified, *viz*

$$F' = \frac{\Delta F}{F_0} \approx \frac{\Delta L}{L_0} = \frac{\frac{1}{2}\rho C_{L\alpha}\Delta\left(\alpha_b V_{rel}^2\right)}{\frac{1}{2}\rho C_{L\alpha}\left(\alpha_{b,0} V_{rel,0}^2\right)} = \frac{\Delta\left(\alpha_b V_{rel}^2\right)}{\alpha_{b,0} V_{rel,0}^2} \tag{3.4}$$

Using a Taylor series approximation, the force perturbation can be simplified further to

$$F' \approx \frac{\Delta V_{rel}^2}{V_{rel,0}^2} + \frac{\Delta\alpha_b}{\alpha_{b,0}} \tag{3.5}$$

The perturbation of the blade forces can be broken down into two parts: the change in the forces due to the change in the relative velocity ($\Delta V_{rel}^2/V_{rel,0}^2$) and the change in the forces due to the change in the blade angle of attack ($\Delta\alpha_b/\alpha_{b,0}$). By assuming small angles and that the rotational velocity is much larger than the v-velocity of the flow, the change in the square of the relative velocity and the change in the angle of attack can be found, *viz*

$$\Delta V_{rel}^2 \approx u^2 - u_\infty^2 + 2v\Omega R \tag{3.6}$$

$$\Delta\alpha_b \approx \frac{u_\infty - u}{\Omega R} \tag{3.7}$$

The freestream velocity (u_∞) is known, the rotational velocity (ΩR) is determined by the tip-speed ratio (λ=8; $\Omega R = \lambda u_\infty$), and the u- and v-velocities are found using PIV.

3.3 Experimental Results

3.3.1 Flow Visualization Results

The flow visualization experiments provide a qualitative analysis of flow separation. The Reynolds number in the water channel is lower than the full-scale Reynolds number, so the full-scale fairing is expected to have less separation than the results shown here. The flow visualization experiments are still useful for comparing the fairing designs.

Figure 3.4 shows the dye images for the C30u airfoil at 0°, 10°, and 20°. At 0° there appears to be a small separation bubble, but otherwise the flow remains attached. At 10° and 20° the flow is separated, with the boundary layer separating almost immediately for the 20° case. Figure 3.5 shows the dye images for the E863 airfoil at 0°, 10°, and 20°. At 0° the boundary layer remains attached, while the flow is separated at 10° and 20°. The boundary layer remains attached longer for the 10° case.

At 0° the C30u has a small separation bubble that the E863 does not have, but the E863 has a thicker boundary layer that would result in a thicker wake. Both airfoils appear to have a similar performance at 10° and 20°. Both airfoils were also observed at 5°, but there was no apparent distinction between the two airfoils. Overall the airfoils appear to perform equally with respect to flow separation, although tests should be run closer to the full-scale Reynolds number to verify this.

3.3.2 Particle Image Velocimetry Results

The PIV experiments were used to analyze the wake of the two airfoils compared to the wake of a cylinder. Figures 3.6, 3.7, and 3.8 show the instantaneous velocity field in the wake of each model at 0°, 10°, and 20° respectively. At 0°, both airfoils have a thin wake with a small velocity deficit, while the cylinder displays a thick wake region with large turbulent eddies. At 10°, both airfoil wakes exhibit turbulent behavior and the wake region is much larger than the 0° case, although they are still smaller than the cylinder wake region. At 20°, the E863 has a larger wake and more turbulence than the 10° case, but the differences are not that great. For the C30u at 20°, the wake region is significantly larger than the 10° case and is close to the size of the cylinder wake. The C30u also has a significant amount of flow acceleration around the top and bottom surfaces of the wake.

The average wake velocities and turbulence contours at 0°, 10°, and 20° are shown in Figs. 3.9, 3.10, and 3.11 respectively. At 0°, both airfoils have a significantly thinner wake and lower turbulence than the cylinder. The cylinder has a region of high turbulence at the location farthest upstream of the interrogation window that slowly dies out farther downstream. The C30u appears to have a thinner wake and lower turbulence than the E863, but the differences are minimal. At 10°, the velocity fields of the two airfoils are similar, with both airfoils exhibiting a recirculation zone. The wake thickness of both airfoils has increased, but they are still thinner than the cylinder wake. At the farthest upstream point, the airfoils have significantly lower turbulence than the cylinder, but the differences are less noticeable farther downstream. The airfoils have similar turbulence levels, but the C30u has less turbulence at the top and bottom of the interrogation window. At 20°, the wake regions of the airfoils are slightly thicker and appear to

be near the thickness of the cylinder wake. The recirculation zone of the C30u is significantly larger than that of the E863, extending approximately half of the interrogation window. Both airfoils wakes exhibit similar turbulence. The turbulence of the cylinder is significantly higher than that of the airfoils in the upstream half of the interrogation window, but the turbulence levels are approximately the same as the airfoils in the downstream half of the interrogation window.

The *u*-velocity profiles at two fixed *X* locations for angles of attack of 0°, 10°, and 20° are shown in Figs. 3.12, 3.13, and 3.14 respectively. At 0°, both airfoils have a very thin wake with a small velocity deficit. The cylinder wake extends nearly the entire height of the interrogation window and has a larger velocity deficit than the airfoils. The C30u appears to have a slightly smaller velocity deficit than the E863. The velocity deficits of the airfoils' wakes are reduced farther downstream, but the velocity deficit of the cylinder appears to remain unchanged downstream. At 10°, both airfoils have a significantly thicker wake and larger velocity deficit than at 0°. The wake thicknesses and velocity deficits appear to be approximately equal for both airfoils. At the farther upstream location, the airfoils have larger velocity deficits than the cylinder, but they also have thinner wakes. At the farther downstream location, the velocity deficit of the airfoils is approximately the same as the velocity deficit of the cylinder, but the airfoils have thinner wakes. At 20°, the airfoils have thicker wakes and larger velocity deficits than at 10°. The C30u has a larger velocity deficit than the E863, but the E863 exhibits asymmetric behavior. The velocity deficits of both airfoils wakes are larger than that of the cylinder at both *X* locations, but the thicknesses of the airfoil wakes are slightly smaller than the cylinder wake.

The *v*-velocity profiles at two fixed *X* locations for angles of attack of 0°, 10°, and 20° are shown in Figs. 3.15, 3.16, and 3.17 respectively. At 0°, all of the models had an average *v*-velocity of zero, but the cylinder has large variations in the velocity that the C30u and E863 do not have. The C30u has a lower deviation from the mean in the airfoil wake than the E863. At 10°, the variation in the *v*-velocity of the airfoils is only slightly less than the variation in the velocity of the cylinder wake, but the variations occur over a thinner region. At the farther upstream location, the average *v*-velocity for both airfoils is negative in the upper half of the interrogation window and positive in the lower half. This effect is reduced farther downstream and is almost gone two diameters downstream. There are no significant differences between the wake velocities of the two airfoils at this angle of attack. At 20°, the variation in the *v*-velocity of both airfoils is on the order of the variation in the velocity of the cylinder wake. The E863 appears to have slightly less variation in the *v*-velocity than the C30u. Similar to the 10° case, the average *v*-velocity for both airfoils is negative in the upper half of the interrogation window and positive in the lower half. This effect is reduced farther downstream but is still present two diameters downstream.

The change in the forces on the turbine blade due to the change in the relative velocity and the change in the blade angle of attack for each of the test cases is shown in Figs. 3.18-3.24. For all cases, the impact of the change in the angle of attack was an order of magnitude larger than the impact of the change in the relative velocity. This means that the change in the angle of attack is the most significant factor to consider when determining the best design for the tower fairing. The downstream location does not appear to have much of an effect on the impact of the cylinder wake, but the impact is reduced for the airfoils at locations farther downstream. The effects due to changes in the relative velocity and angle of attack are by far the smallest for the

two airfoils at 0°. At 10°, the effects are approximately the same for the two airfoils. At the farther upstream location, the airfoils have a larger impact on the blade loads than the cylinder, but at the farther downstream location, the effect of the airfoils is approximately the same as that of the cylinder. At 20°, the E863 appears to have a lower change in the blade loading due to the change in relative velocity than the C30u. The magnitudes of the impact due to the change in angle of attack of the E863 and C30u are approximately the same, but the E863 has an asymmetric distribution. At both downstream locations, the airfoils have a larger impact on the blade loading than the cylinder.

3.4 Conclusions

Flow visualization and PIV were used to analyze flow separation and wake effects of two airfoils at 0°, 10°, and 20°. The flow visualization results showed that both the C30u and E863 airfoils had similar performances with respect to flow separation. At 0°, the flow remained attached, but at 10° and 20°, the flow separated almost immediately for both airfoils. The Reynolds number for the experiments is two orders of magnitude less than the full-scale Reynolds number, so the flow is more likely to remain attached for the full-scale fairing. At 0°, the C30u appeared to have a small separation bubble that the E863 did not have, but the E863 had a thicker boundary layer than the C30u. Other than those differences at 0°, the dye experiments showed no discernable differences between the two airfoils. Further tests with a Reynolds number closer to the full-scale would be useful to distinguish the two airfoils.

From the PIV results it appeared that there were few differences between the performances of the C30u and E863 airfoils. At 0°, the C30u appeared to perform slightly better than the E863,

while the E863 appeared to perform slightly better at 20°. At 10°, both airfoils appeared to have approximately equal performances.

The wake effects of the C30u and E863 airfoils were significantly lower than the cylinder wake effects at 0°. At 10°, the airfoils performed slightly better than the cylinder, but the advantages of the tower shroud are not as pronounced at this angle of attack as they are at 0°. The cylinder actually appeared to have a slightly better performance at an angle of attack of 20°. Due to the self-aligning nature of the fairing it should not experience large angles of attack for long periods of time. One of the main factors for the reduced performance of the airfoils compared to the cylinder at higher angles of attack is most likely due to the flow separation that was observed in the dye experiments. At the full-scale Reynolds number, the flow around the airfoils is more likely to remain attached, while the flow around the cylinder may still separate. Experimental testing at higher Reynolds numbers is suggested to better predict the performance of the tower fairing designs.

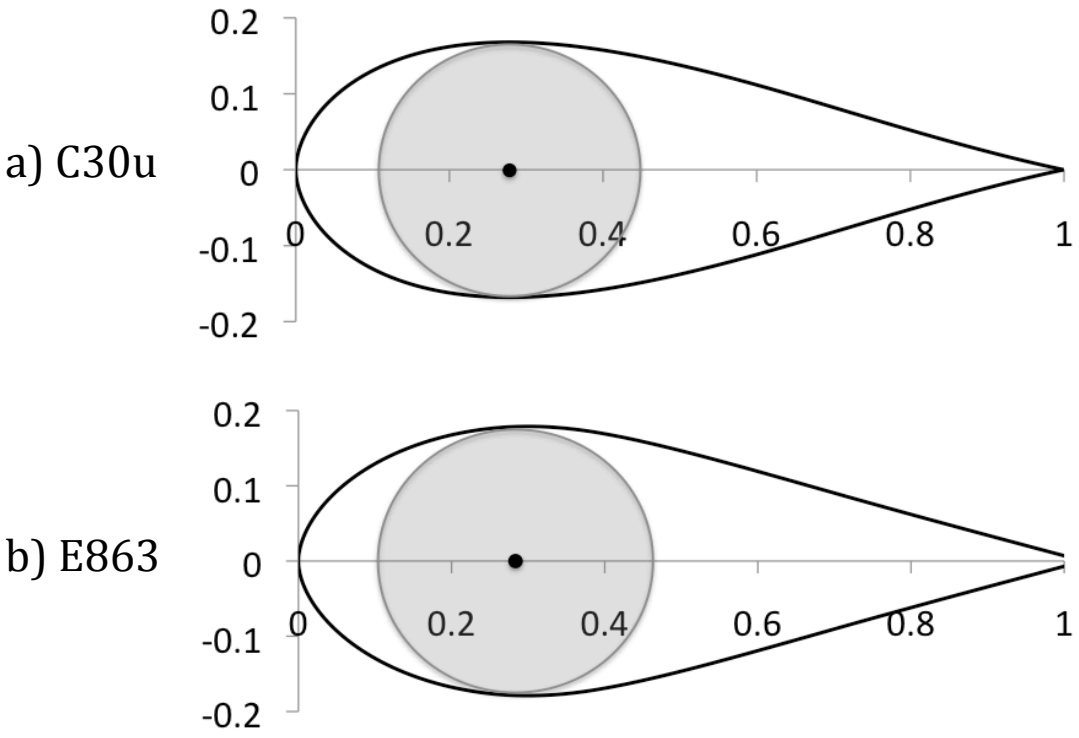

Figure 3.1: Schematics of the selected airfoils with the tower located at the maximum thickness.

a)

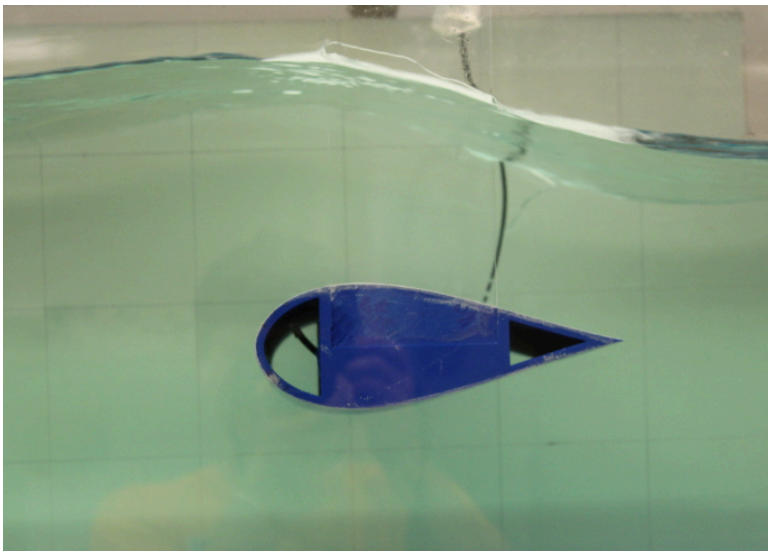

b)

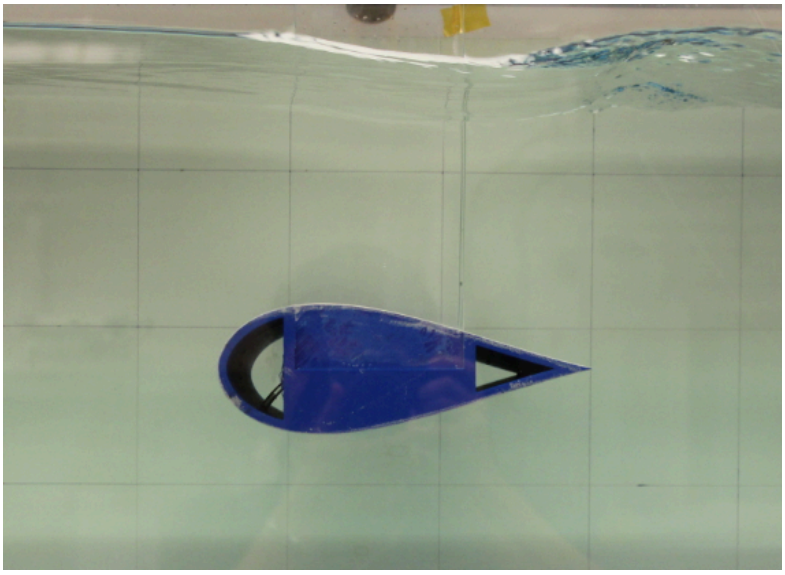

Figure 3.2: Water channel free surface effect at a) 0.8 m/s, and b) 0.5 m/s.

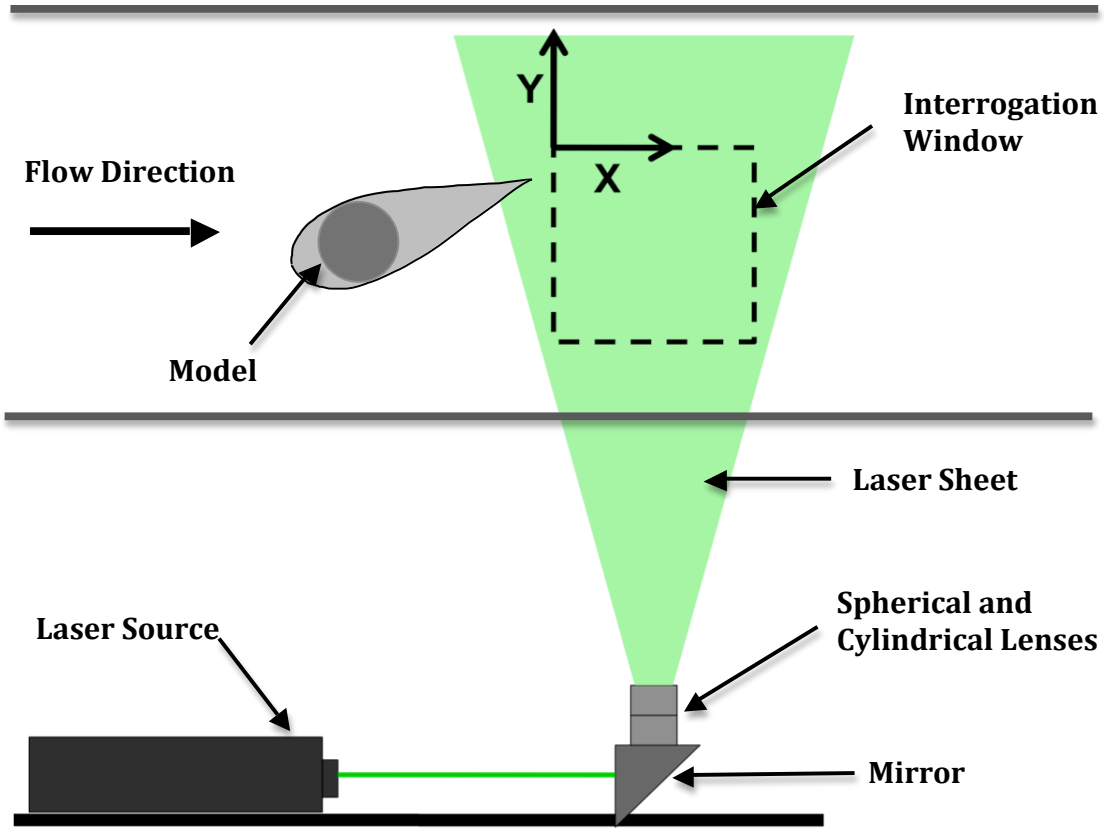

Figure 3.3: Schematic of PIV Setup.

Table 3.1: PIV System

Laser	
Manufacturer	New Wave
Model	Nd: Yag Solo PIV III
Pulse Duration	3-5 ns
Pulse Frequency	7 Hz
Pulse Energy	150 mJ
Camera	
Manufacturer	TSI
Model	PowerView Plus
Resolution	2048x2048
Processing	
Software	Insight 4G
Method	Two Image Cross Correlation
Grid	Nyquist
Spot Size	64x64

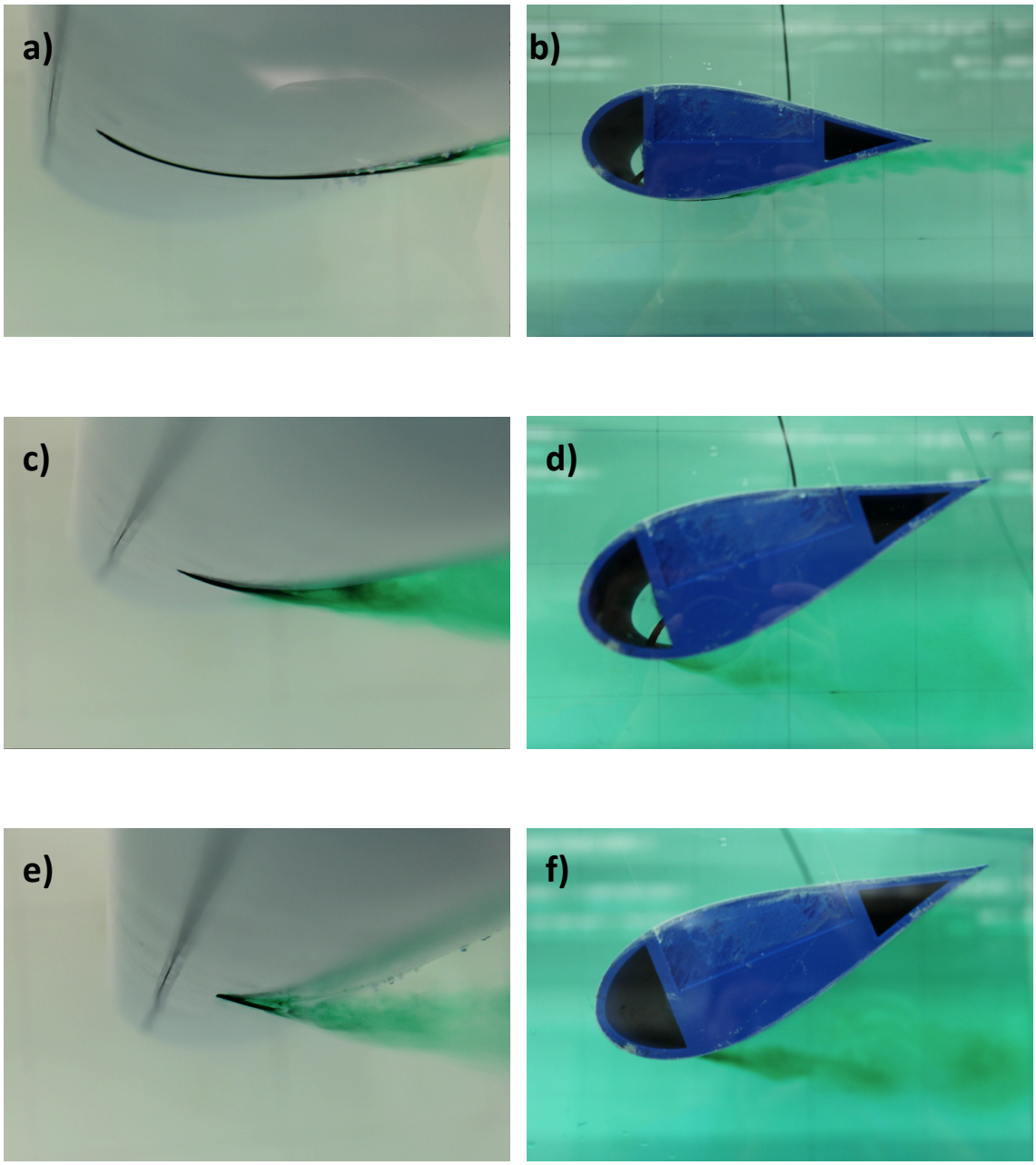

Figure 3.4: Dye images for the C30u at: a) 0°, zoomed in, b) 0°, zoomed out, c) 10°, zoomed in, d) 10°, zoomed out, e) 20°, zoomed in, and f) 20°, zoomed out.

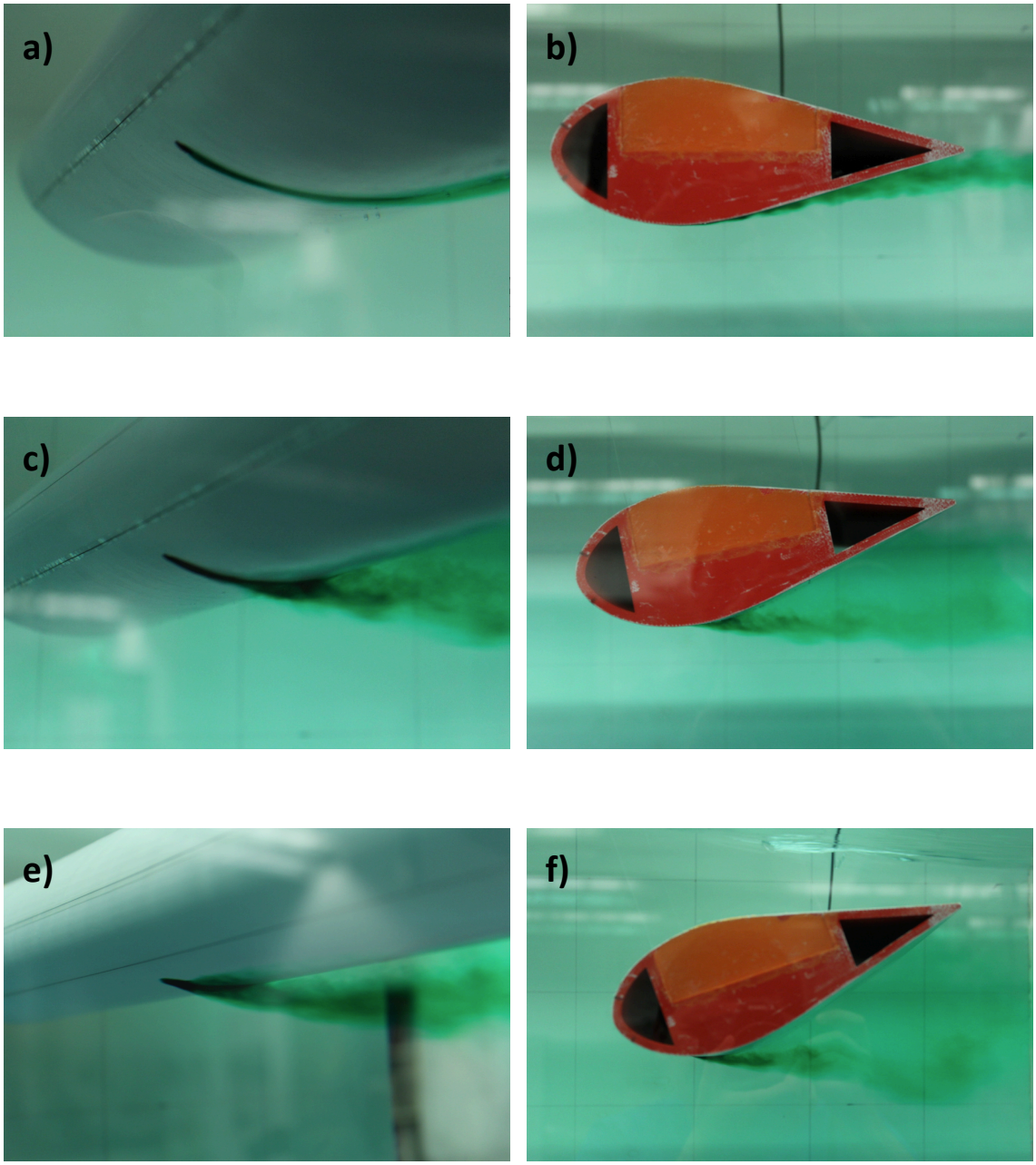

Figure 3.5: Dye images for the E863 at: a) 0°, zoomed in, b) 0°, zoomed out, c) 10°, zoomed in, d) 10°, zoomed out, e) 20°, zoomed in, and f) 20°, zoomed out.

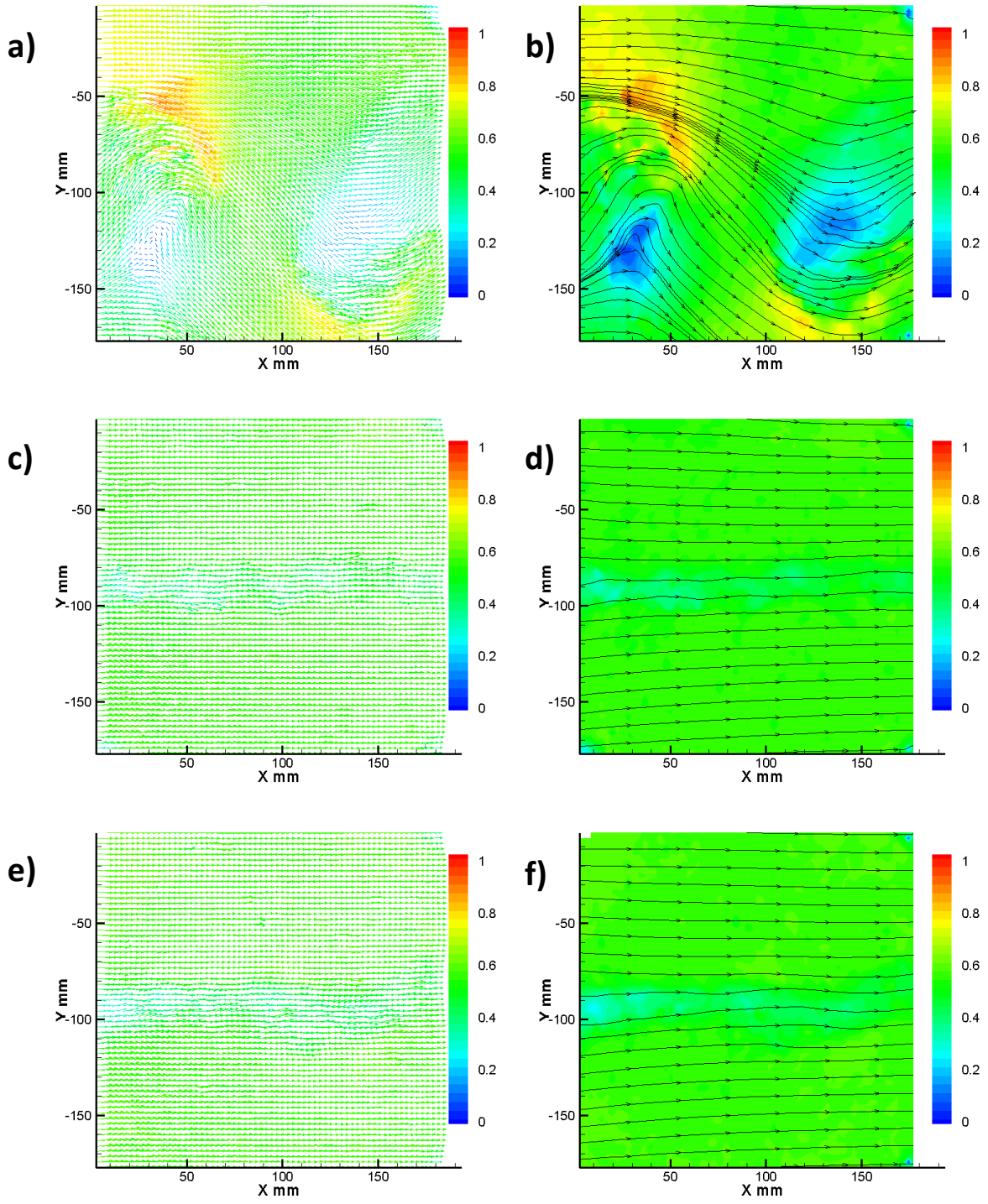

Figure 3.6: Instantaneous velocity vectors and contours at 0° for a-b) the cylinder, c-d) the C30u airfoil, and e-f) the E863 airfoil.

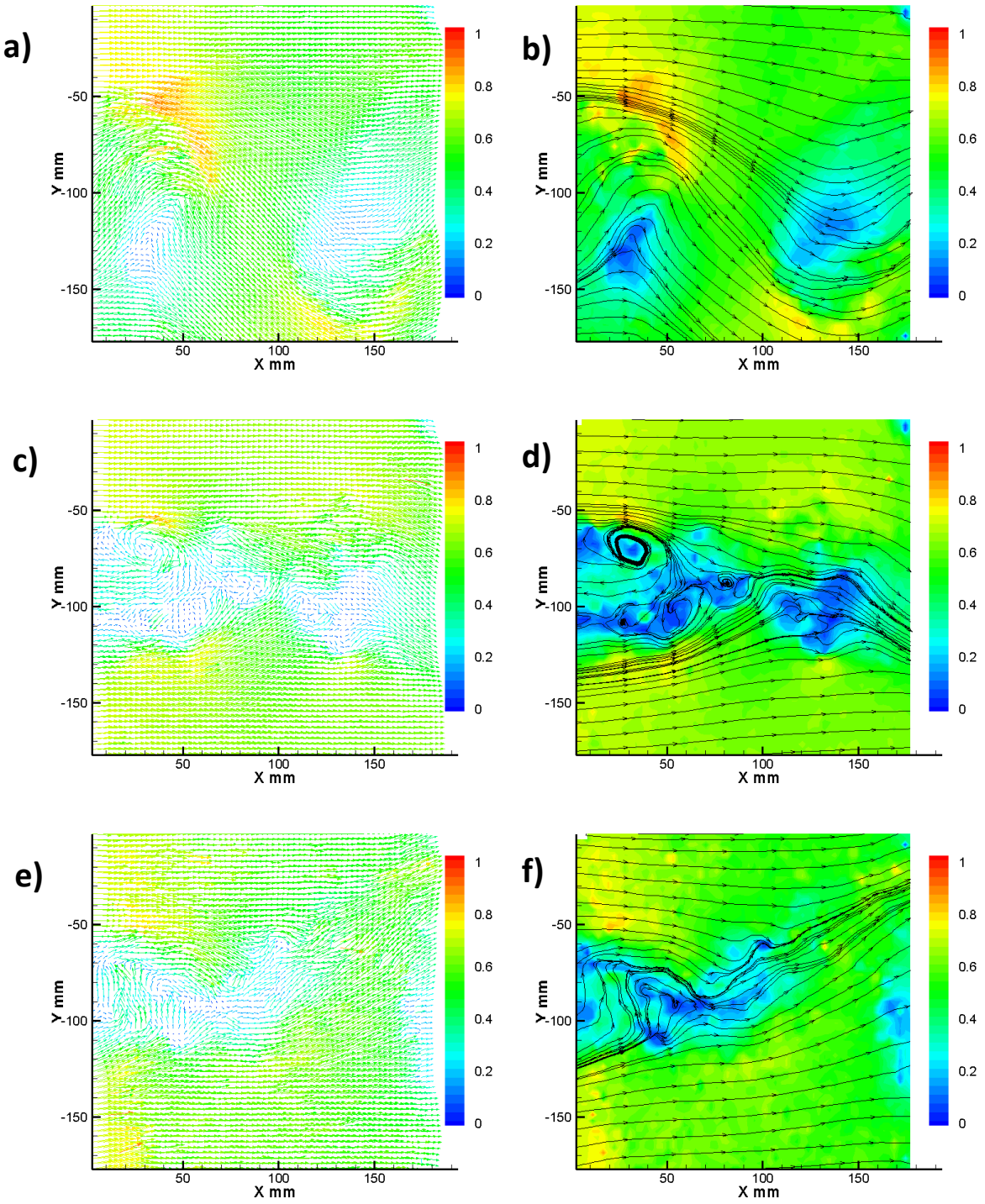

Figure 3.7: Instantaneous velocity vectors and contours at 10° for a-b) the cylinder, c-d) the C30u airfoil, and e-f) the E863 airfoil.

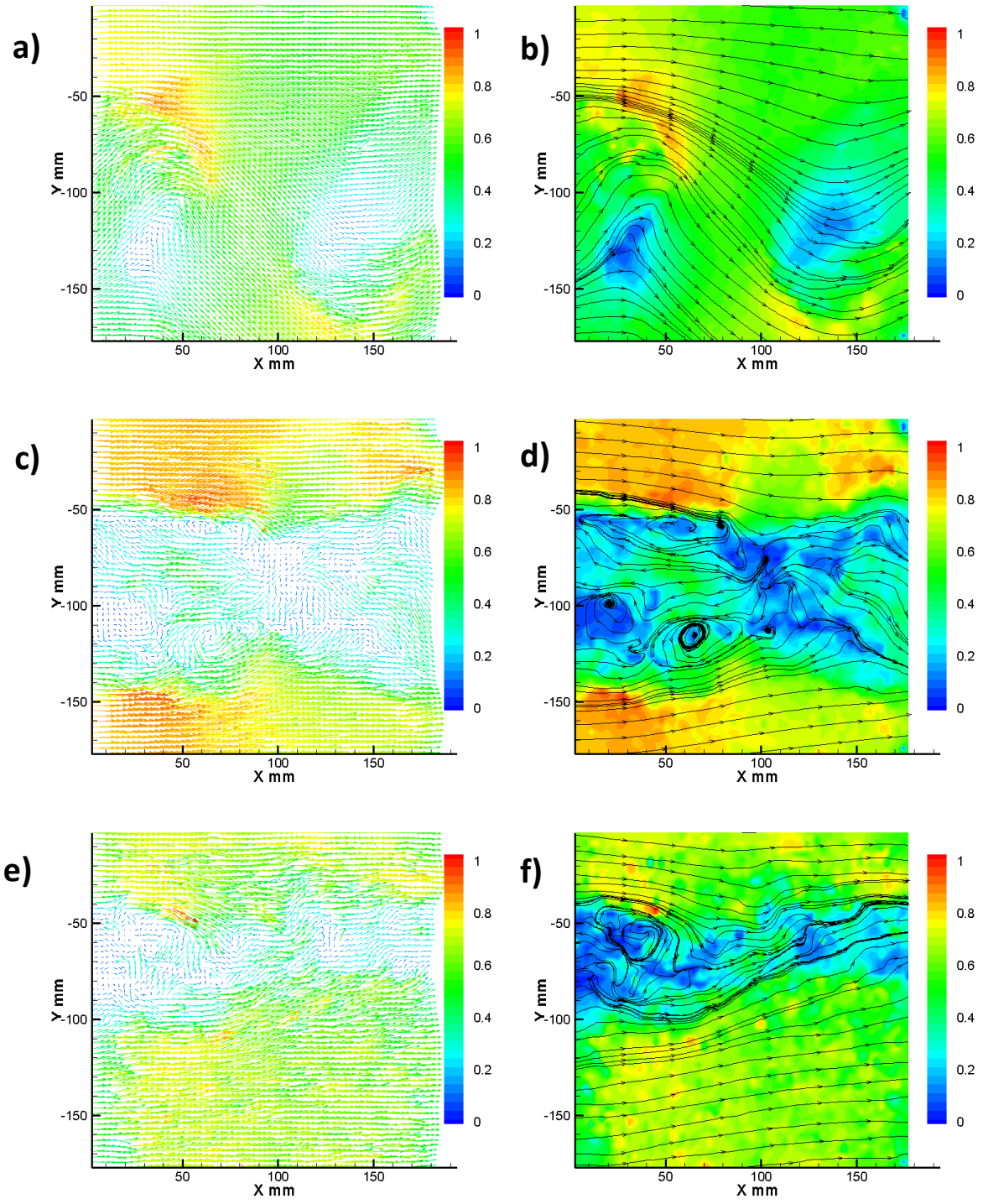

Figure 3.8: Instantaneous velocity vectors and contours at 20° for a-b) the cylinder, c-d) the C30u airfoil, and e-f) the E863 airfoil.

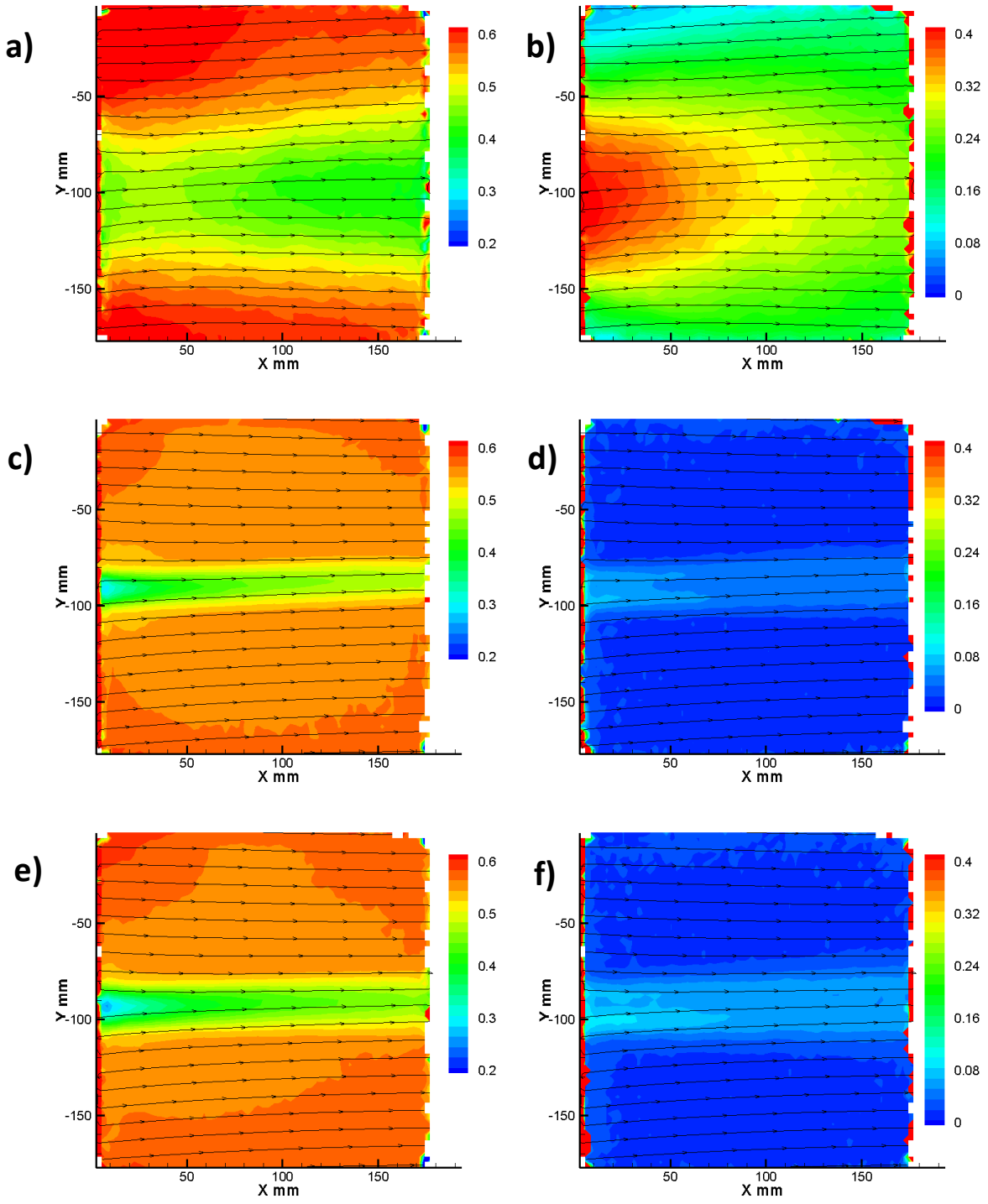

Average velocity contours (m/s) Average turbulence contours (m/s)

Figure 3.9: Average velocity and turbulence contours at 0° for a-b) the cylinder, c-d) the C30u airfoil, and e-f) the E863 airfoil.

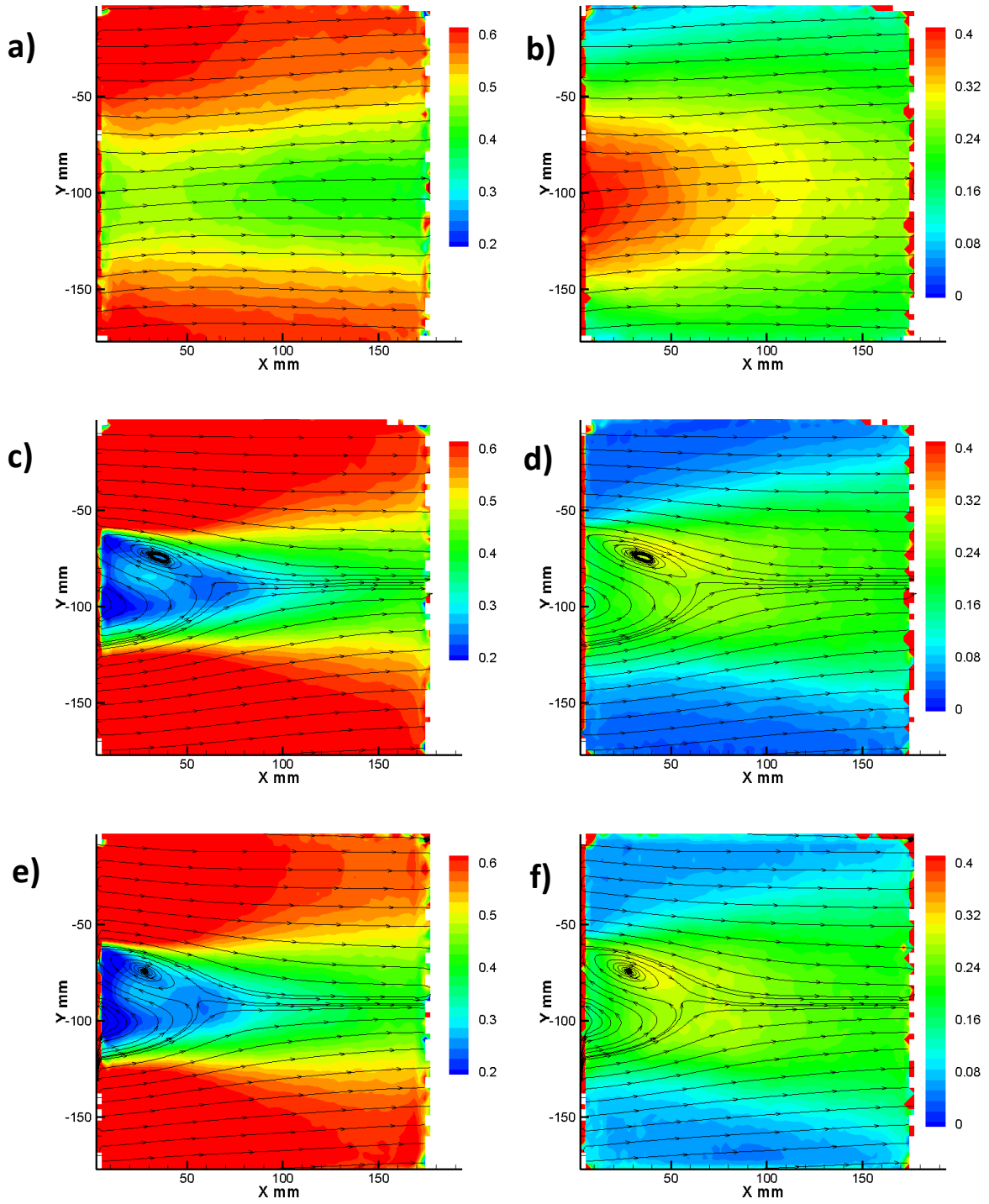

Average velocity contours (m/s) Average turbulence contours (m/s)

Figure 3.10: Average velocity and turbulence contours at 10° for a-b) the cylinder, c-d) the C30u airfoil, and e-f) the E863 airfoil.

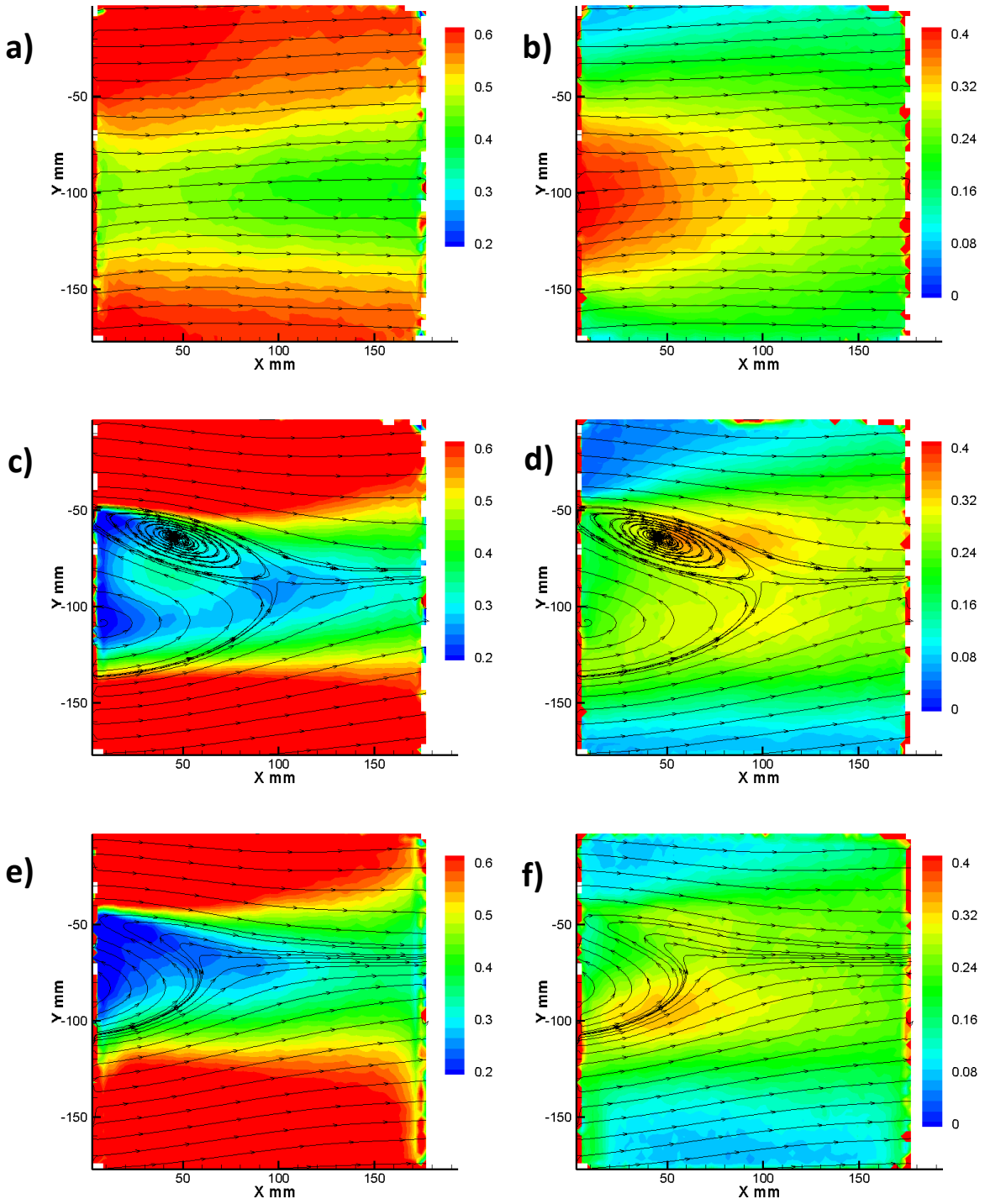

Average velocity contours (m/s) Average turbulence contours (m/s)

Figure 3.11: Average velocity and turbulence contours at 20° for a-b) the cylinder, c-d) the C30u airfoil, and e-f) the E863 airfoil.

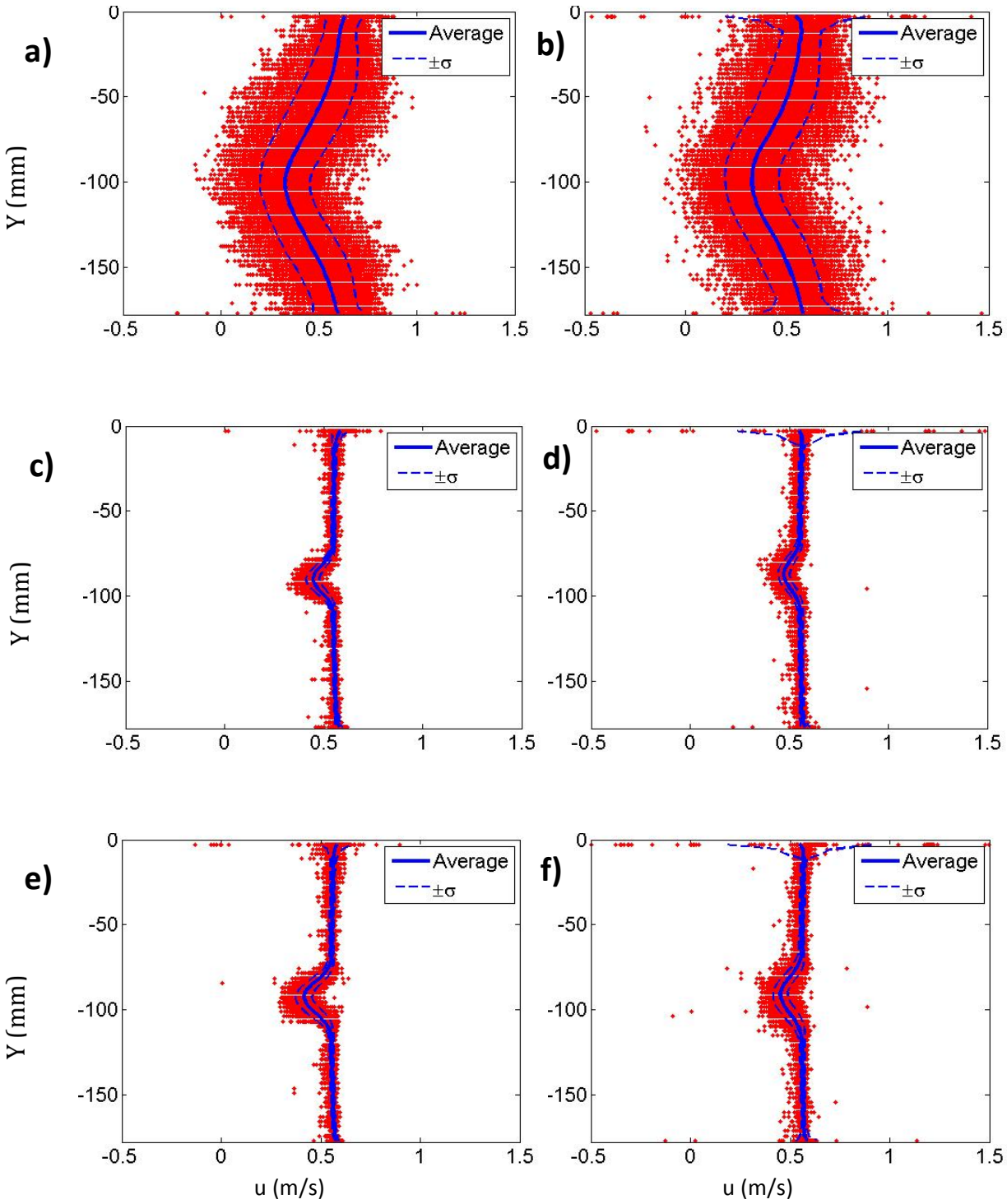

Figure 3.12: u-velocity profile at 0° a) one diameter downstream for the cylinder, b) two diameters downstream for the cylinder, c) one diameter downstream for the C30u airfoil, d) two diameters downstream for the C30u airfoil, e) one diameter downstream for the E863 airfoil, and f) two diameters downstream for the E863 airfoil.

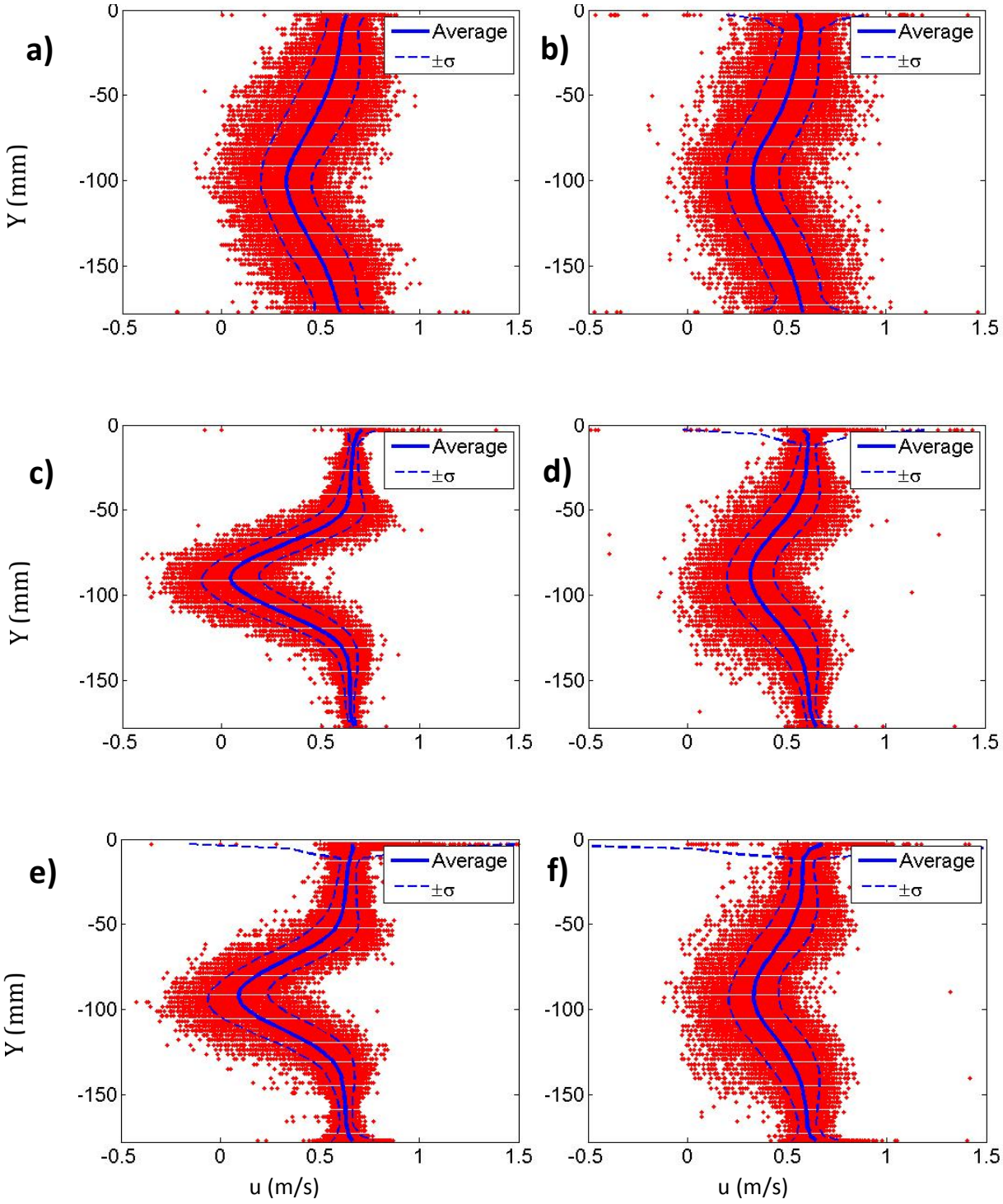

Figure 3.13: u-velocity profile at 10° a) one diameter downstream for the cylinder, b) two diameters downstream for the cylinder, c) one diameter downstream for the C30u airfoil, d) two diameters downstream for the C30u airfoil, e) one diameter downstream for the E863 airfoil, and f) two diameters downstream for the E863 airfoil.

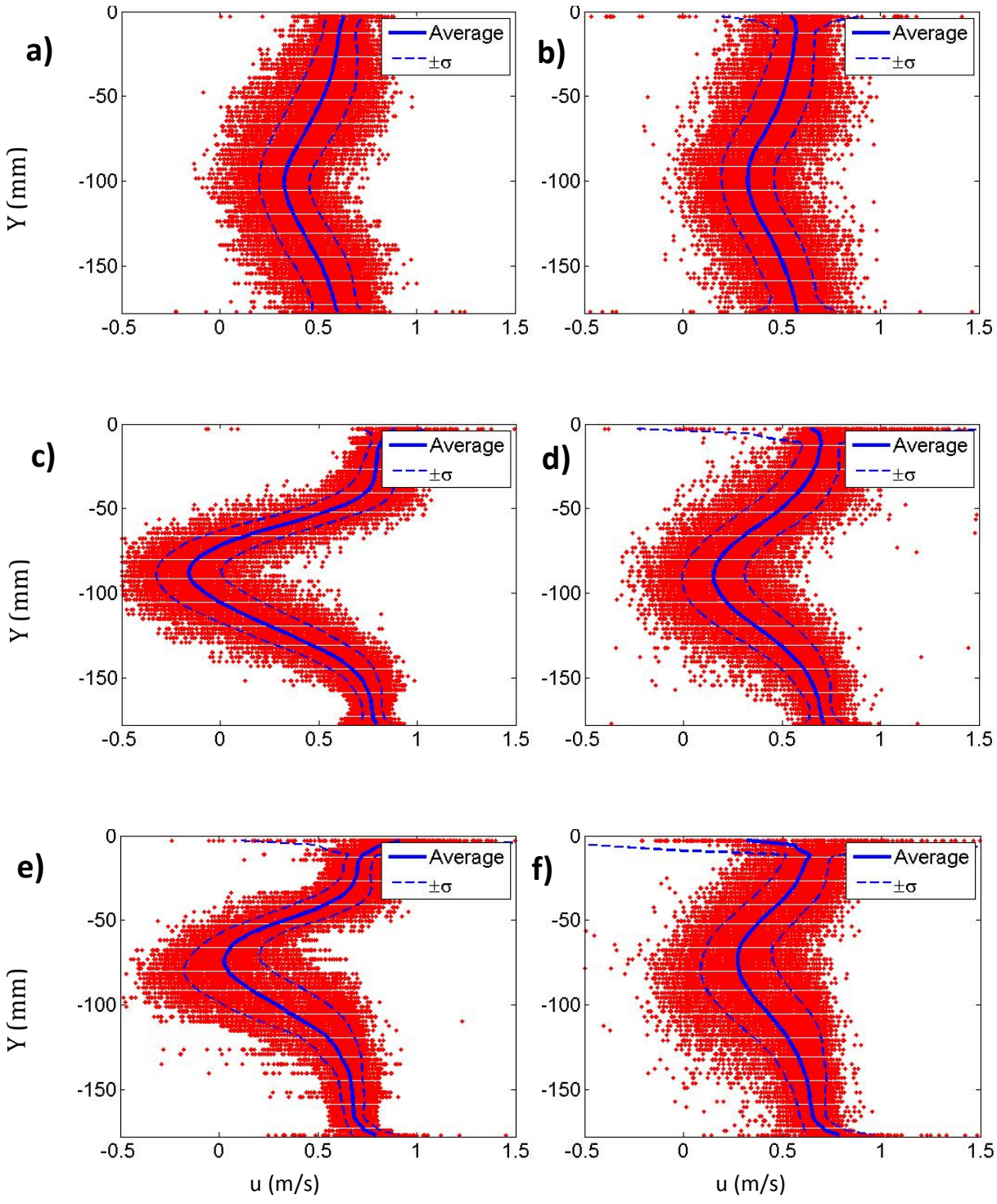

Figure 3.14: u-velocity profile at 20° a) one diameter downstream for the cylinder, b) two diameters downstream for the cylinder, c) one diameter downstream for the C30u airfoil, d) two diameters downstream for the C30u airfoil, e) one diameter downstream for the E863 airfoil, and f) two diameters downstream for the E863 airfoil.

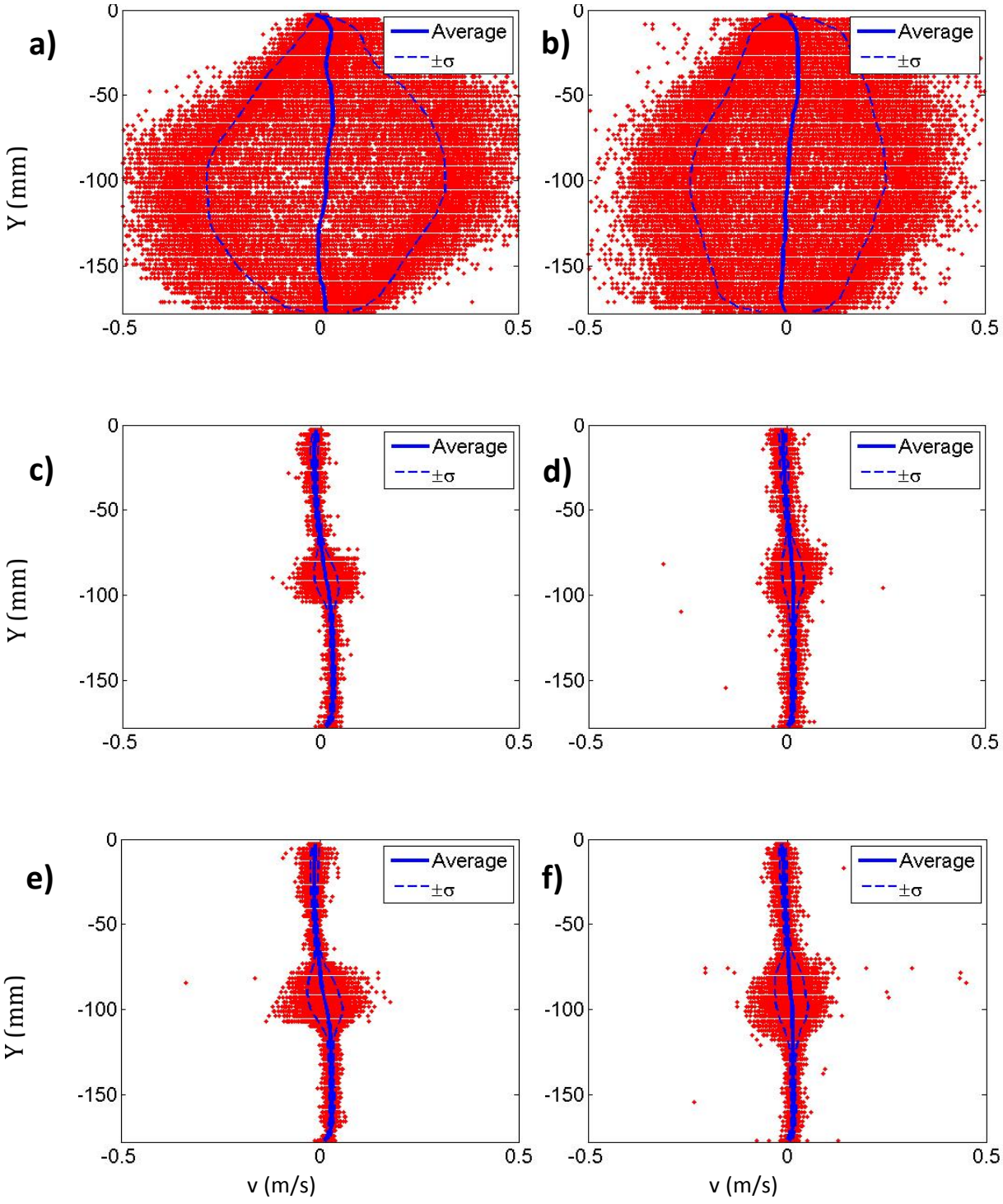

Figure 3.15: v-velocity profile at 0° a) one diameter downstream for the cylinder, b) two diameters downstream for the cylinder, c) one diameter downstream for the C30u airfoil, d) two diameters downstream for the C30u airfoil, e) one diameter downstream for the E863 airfoil, and f) two diameters downstream for the E863 airfoil.

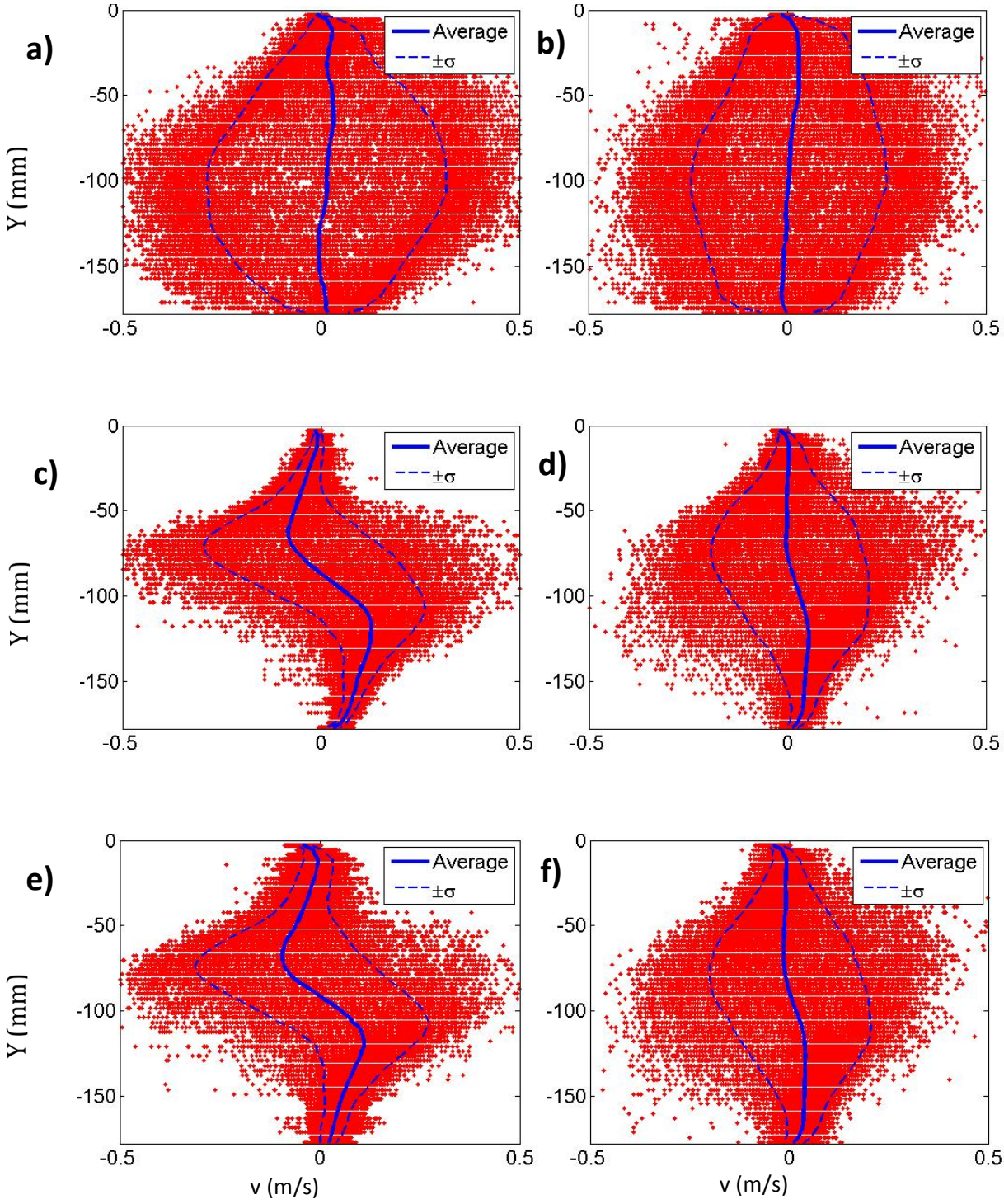

Figure 3.16: v-velocity profile at 10° a) one diameter downstream for the cylinder, b) two diameters downstream for the cylinder, c) one diameter downstream for the C30u airfoil, d) two diameters downstream for the C30u airfoil, e) one diameter downstream for the E863 airfoil, and f) two diameters downstream for the E863 airfoil.

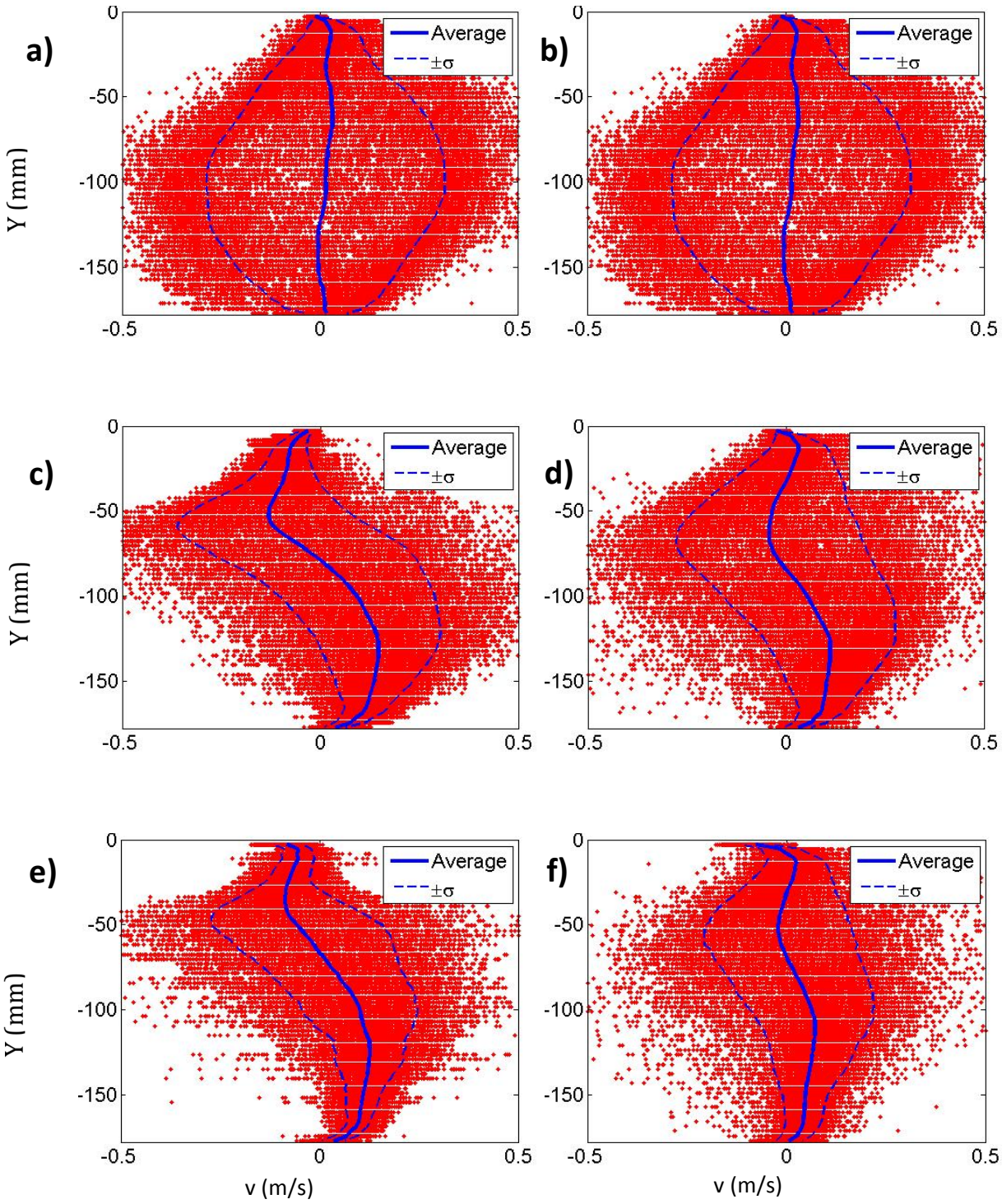

Figure 3.17: v-velocity profile at 20° a) one diameter downstream for the cylinder, b) two diameters downstream for the cylinder, c) one diameter downstream for the C30u airfoil, d) two diameters downstream for the C30u airfoil, e) one diameter downstream for the E863 airfoil, and f) two diameters downstream for the E863 airfoil.

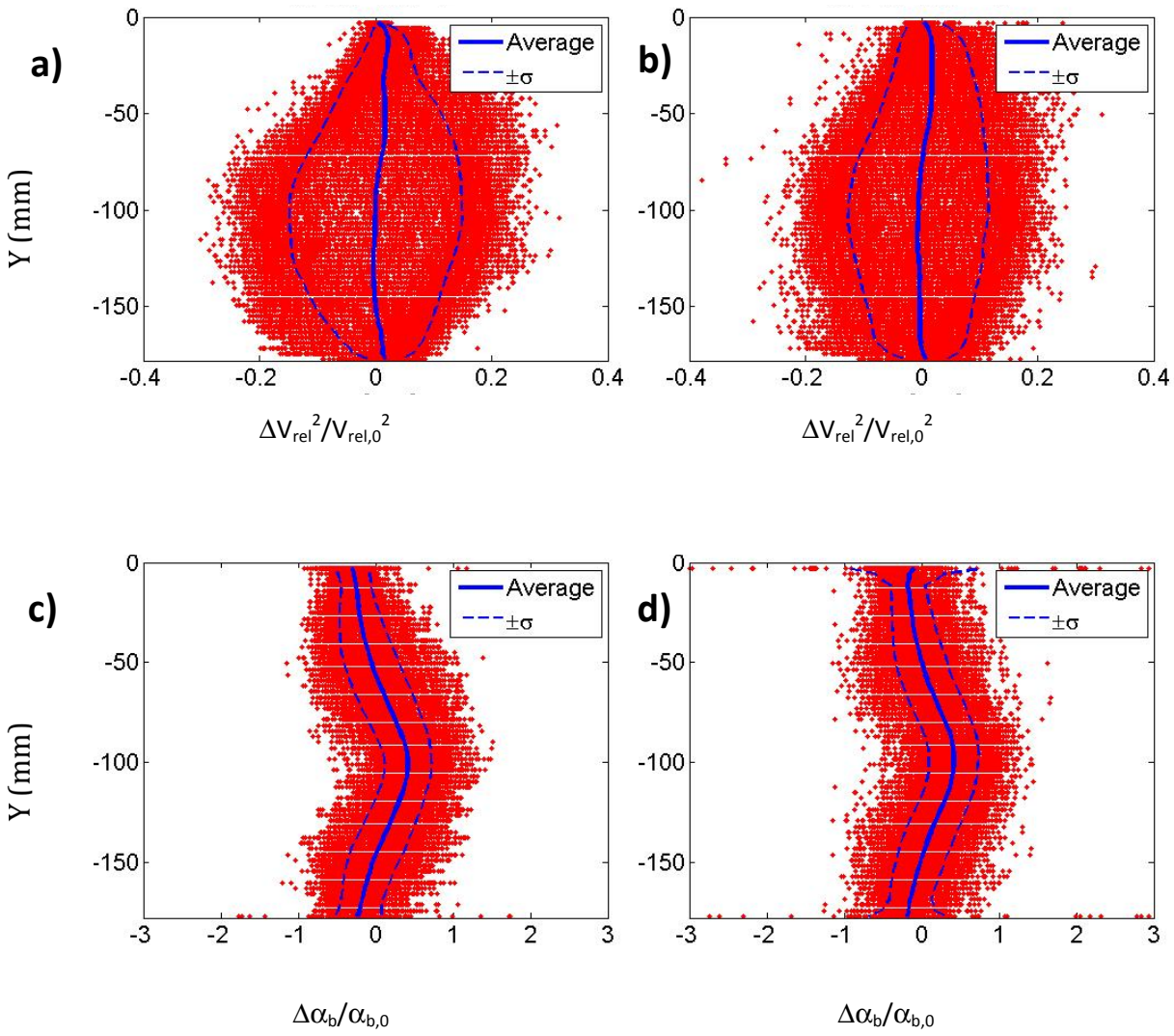

Figure 3.18: Wake perturbation for the cylinder due to a) the relative velocity change one diameter downstream, b) the relative velocity change two diameters downstream, c) the change in angle of attack one diameter downstream, and d) the change in angle of attack two diameters downstream.

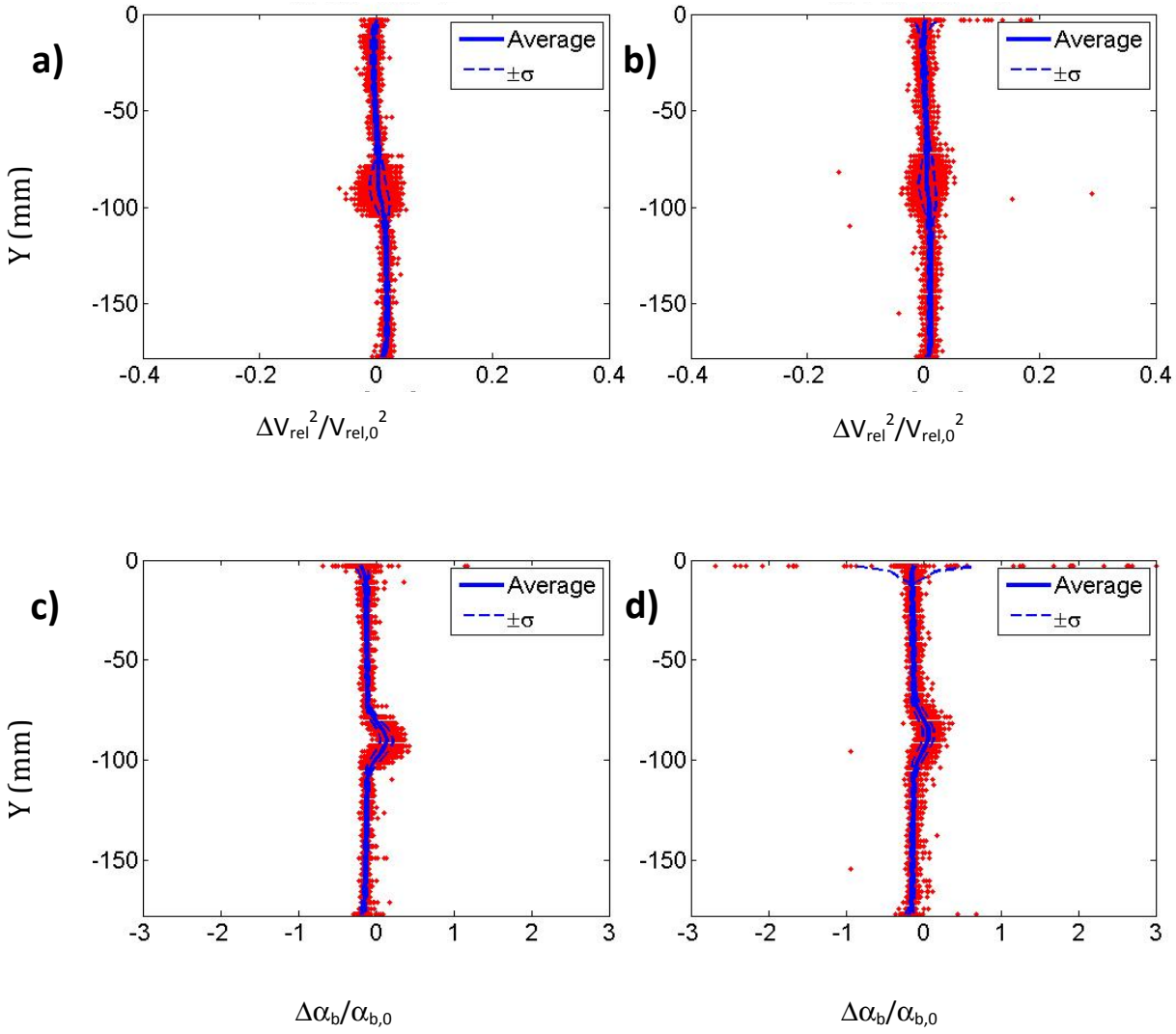

Figure 3.19: Wake perturbation for the C30u airfoil at 0° due to a) the relative velocity change one diameter downstream, b) the relative velocity change two diameters downstream, c) the change in angle of attack one diameter downstream, and d) the change in angle of attack two diameters downstream.

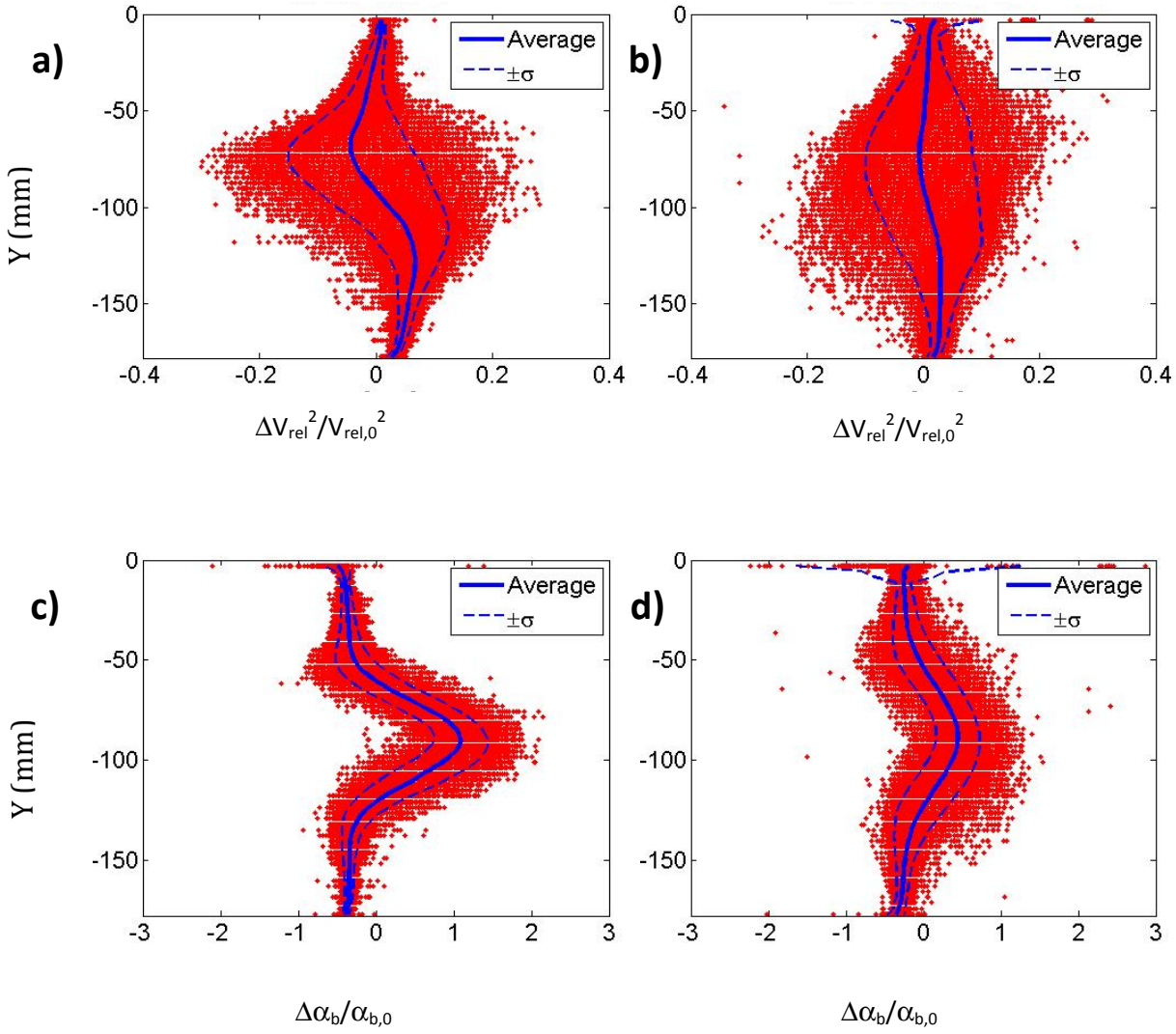

Figure 3.20: Wake perturbation for the C30u airfoil at 10° due to a) the relative velocity change one diameter downstream, b) the relative velocity change two diameters downstream, c) the change in angle of attack one diameter downstream, and d) the change in angle of attack two diameters downstream.

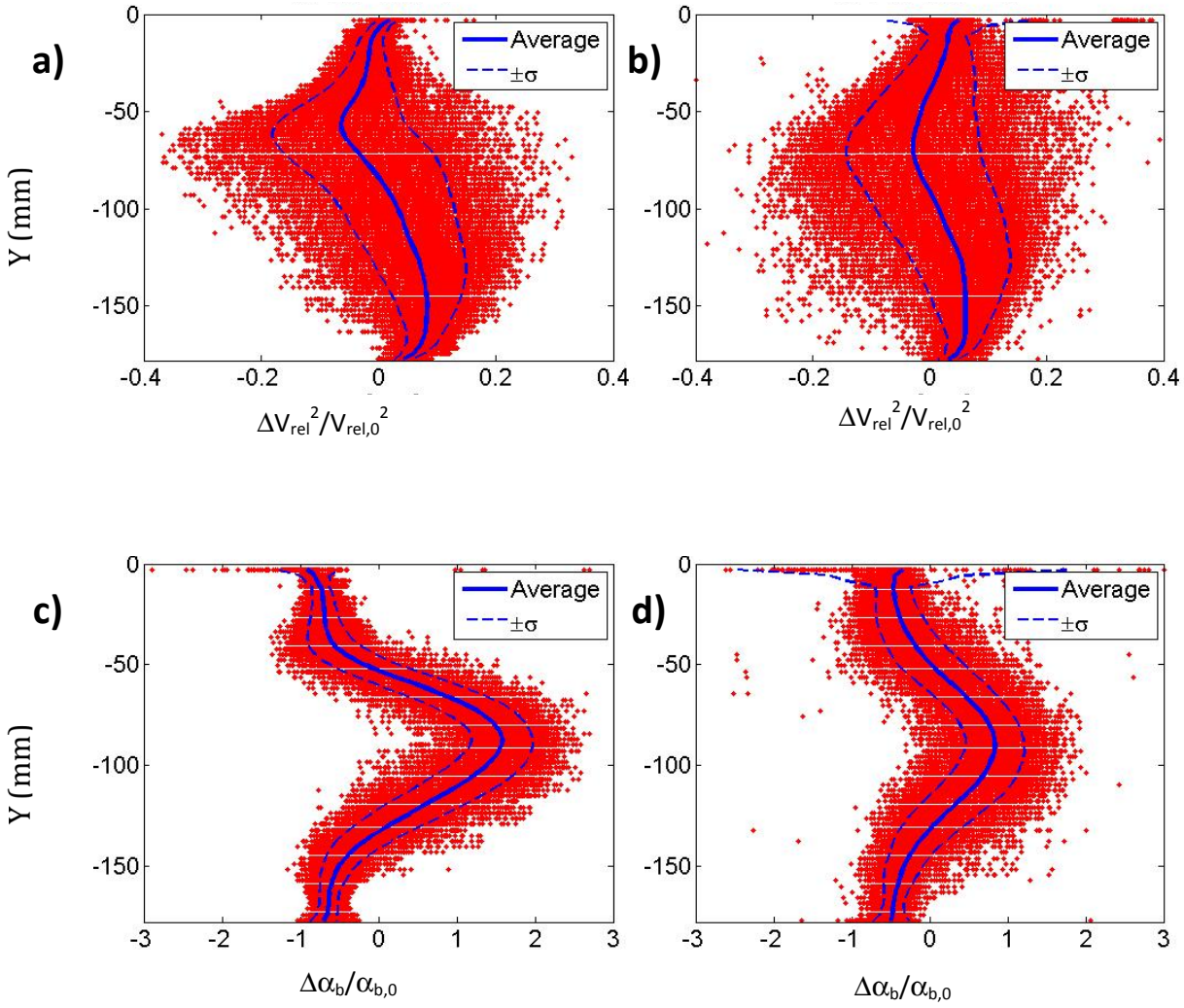

Figure 3.21: Wake perturbation for the C30u airfoil at 20° due to a) the relative velocity change one diameter downstream, b) the relative velocity change two diameters downstream, c) the change in angle of attack one diameter downstream, and d) the change in angle of attack two diameters downstream.

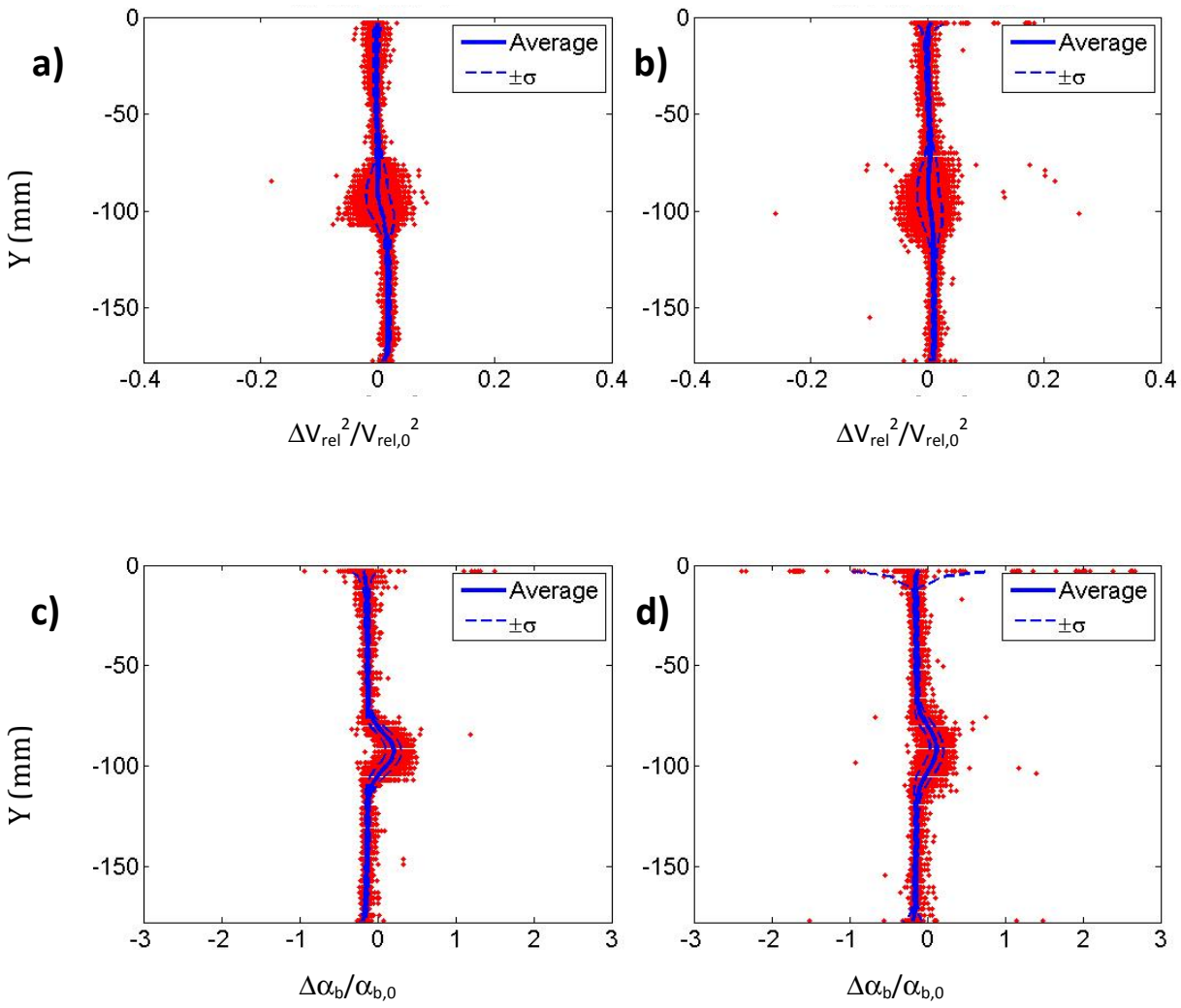

Figure 3.22: Wake perturbation for the E863 airfoil at 0° due to a) the relative velocity change one diameter downstream, b) the relative velocity change two diameters downstream, c) the change in angle of attack one diameter downstream, and d) the change in angle of attack two diameters downstream.

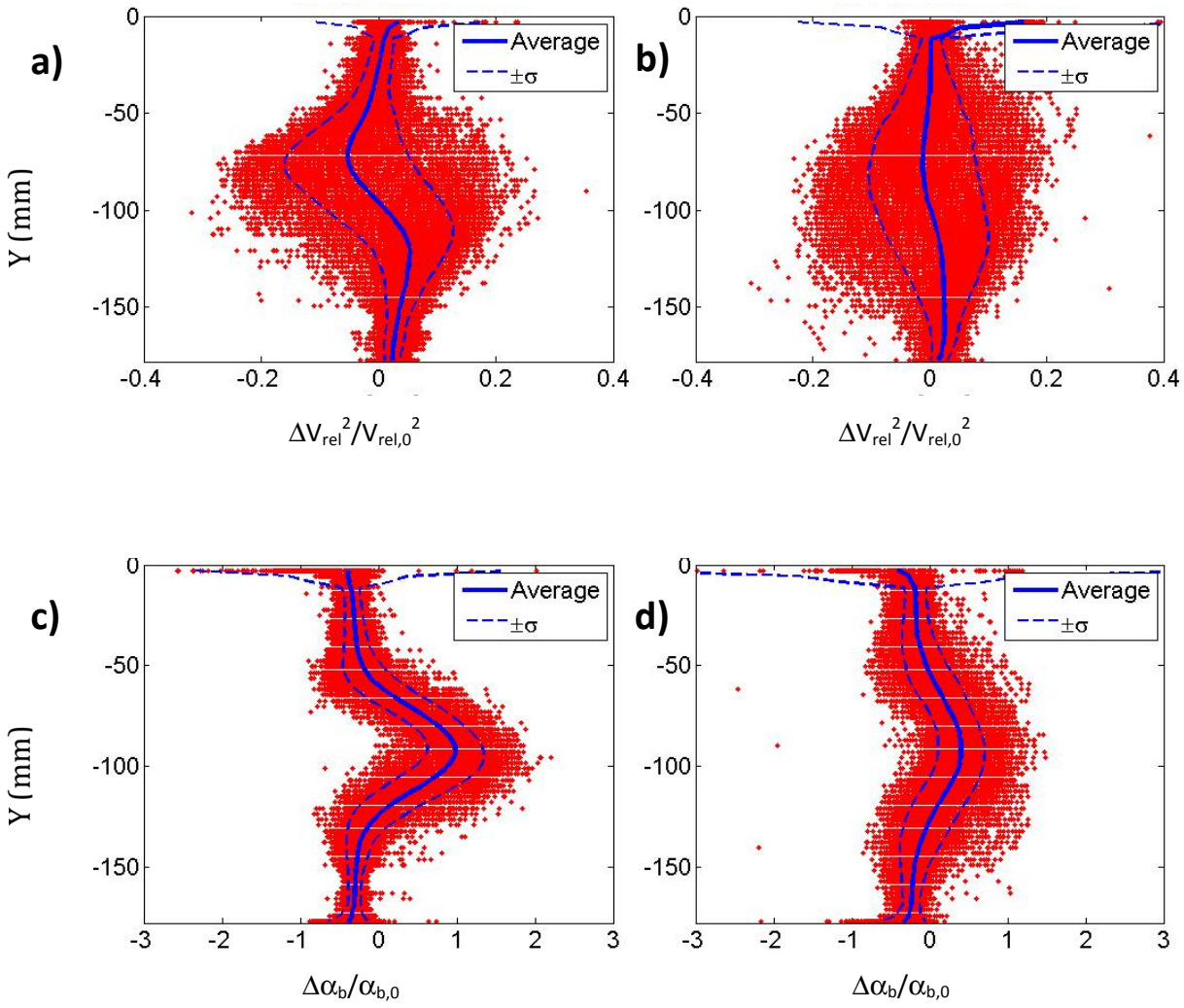

Figure 3.23: Wake perturbation for the E863 airfoil at 10° due to a) the relative velocity change one diameter downstream, b) the relative velocity change two diameters downstream, c) the change in angle of attack one diameter downstream, and d) the change in angle of attack two diameters downstream.

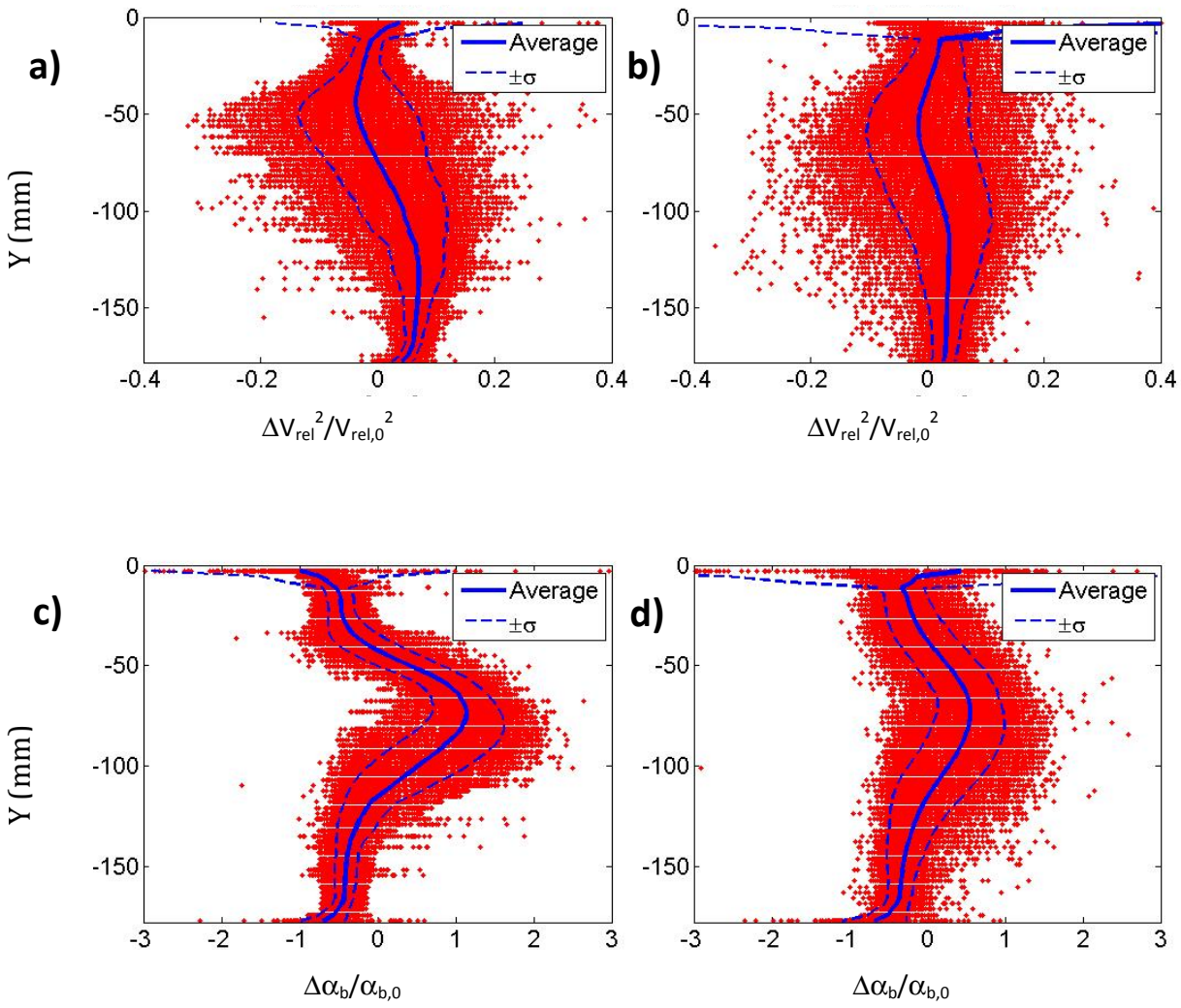

Figure 3.24: Wake perturbation for the E863 airfoil at 20° due to a) the relative velocity change one diameter downstream, b) the relative velocity change two diameters downstream, c) the change in angle of attack one diameter downstream, and d) the change in angle of attack two diameters downstream.

Chapter 4

Dynamic Scaling Considerations

4.1 Introduction

Due to the high cost of building a full-scale wind turbine, experimental tests must first be conducted using scaled models. In addition to geometric scaling, proper dynamic scaling is a critical element of the experimental tests. Experiments may be performed in both the NASA Ames wind tunnel and a water channel located at the University of Virginia. Testing the static and dynamic fluid-elastic properties of the wind turbine requires careful consideration of the forces (gravity, centrifugal, and thrust) and system frequencies (e.g. convection, rotation, inertial, and stiffness-based structural frequencies). While the Mach and Reynolds numbers of the models cannot be matched to the full-scale values, specific parameters must be held constant to ensure the correct fluid dynamics, load distributions, and tower and blade dynamics.

Designing a dynamically scaled model of an extreme-scale wind turbine is challenging, particularly because of the large geometric scaling factor required. This has resulted in a limited number of experiments that employ proper dynamic scaling, especially for scaling factors of this magnitude (rotor diameter on the order of 200 m to a rotor diameter on the order of 1 m or less). Despite the significant challenges, purely aerodynamic models of wind turbines have been developed by, among others, Bottasso *et al.*[27] at the Politecnico di Milano.

To determine the typical loads on the turbine blades, the forces that act on the blade can be decomposed, as shown in Fig. 4.1. According to Loth *et al.*[2], these forces include the gravity force (G), the centrifugal force (C), the downstream aerodynamic thrust force (T), and the in-plane aerodynamic torque-wise force (F_Q).

The load-path angle can be estimated in terms of these forces and the azimuthal blade angle (φ, defined as 0 for a blade that is pointed vertically upwards and π for a blade that is downwards), *viz*

$$\beta = \tan^{-1}\left(\frac{T}{C - G\cos\varphi}\right) \tag{4.1}$$

The Lock number represents the ratio of aerodynamic to inertial forces. Similarly the Froude number represents the ratio of aerodynamic to gravitational forces. As long as these non-dimensional parameters are matched between the full- and model-scale turbines, the load distributions, and therefore the load-path angle, will also be matched.

The angular speed can be expressed in terms of the wind speed (V), the turbine power generating conditions (cut-in, rated, and cut-out), the rotor radius (R), and the optimum tip-speed ratio (λ), *viz*

$$\Omega = 0 \qquad \text{for } V < V_{cut\text{-}in} \tag{4.2}$$

$$\Omega = \lambda V/R \qquad \text{for } V_{cut\text{-}in} < V < V_{rated} \tag{4.3}$$

$$\Omega = \lambda V_{rated}/R = \text{const.} \qquad \text{for } V_{rated} < V < V_{cut\text{-}out} \tag{4.4}$$

$$\Omega = 0 \qquad \text{for } V > V_{cut\text{-}out} \tag{4.5}$$

The tip-speed ratio is typically set to a high value to optimize efficiency and is herein set as λ=8 for off-shore conditions. The rated wind speed controls the maximum power and is herein

set as 12.5 m/s for the full-scale turbine. The rated wind speed is the speed that is used in the scaling calculations.

4.2 Scaling Methodology

The simplest scaling method would be to scale all of the velocities and model dimensions, such as blade radius, blade chord, tower diameter, and tower height, by a single scaling ratio. Unfortunately, this method does not capture the tower and blade dynamics that are needed to accurately model the full-scale wind turbine system. To accurately describe the system, certain non-dimensional scaling parameters must be matched between the model- and full-scale turbines. These parameters are dependent on the length scaling factor defined as

$$\eta \equiv \frac{R_m}{R_p} \tag{4.6}$$

where R is the rotor radius, and the subscripts m and p refer to the (scaled) model and physical (full scale) systems respectively.

The important scaling parameters to consider are the tip-speed ratio ($\lambda=\Omega R/V$), Reynolds number ($Re=\rho Vc/\mu$), Mach number ($M=V/a$), Lock number ($Lo=C_{l\alpha}\ \rho cR^4/J$), Froude number ($Fr=V^2/gR$), and non-dimensional flapping frequency ($\omega_{flap}=\omega_{flap}/\Omega$), where Ω is the rotor angular speed, V is the flow speed, ρ is the density of the fluid, μ is the fluid dynamic viscosity, a is the speed of sound, $C_{l\alpha}$ is the slope of lift curve for the blade, c is the blade chord, J is the flapping inertia of the blade, g is the gravitational acceleration, and ω is the structural natural frequency. For proper fluid dynamic scaling all of these parameters would be matched exactly, but based on flow speed and size constraints in the wind tunnel and water channel, the Reynolds number and Mach number were unable to be matched. The tip-speed ratio, Lock number, Froude

number, and non-dimensional flapping frequency were kept constant between the full- and model-scales.

The Lock number represents the ratio of aerodynamic to inertial forces and is used to calculate the scaled blade mass. It was assumed that the slope of the lift curve was constant between the two scales and the blade chord scaled with the radius. The flapping inertia is proportional to the blade mass times the radius squared. Setting the Lock numbers equal to each other and solving for the blade mass results in

$$m_{blade,m} = \frac{\rho_{fluid}}{\rho_{air}} \eta^3 m_{blade,p} \tag{4.7}$$

The Froude number represents the ratio of aerodynamic to gravitational forces and is used to calculate the flow speed. For the water channel, one must take into account the inertia of the displaced fluid, which is negligible for the air. Setting the Froude numbers equal and solving for the model velocity results in

$$V_m = V_p \sqrt{\eta \left(1 - \frac{\rho_{fluid}}{\rho_{blade}} \right)} \tag{4.8}$$

The density ratio was assumed to be 1/8 for the water channel model, consistent with the density ratio between water and steel. The high density of the blades is necessary to achieve the required blade mass while maintaining a reasonable blade volume. The density ratio is negligible for the wind tunnel model.

The tip-speed ratio is used to calculate the rotor angular speed. The blade radius is fixed, and the flow velocity was found previously, so the rotor speed can then be calculated, *viz*

$$\Omega_m = \Omega_p \frac{1}{\eta} \frac{V_m}{V_p} \tag{4.9}$$

The non-dimensional flapping frequency is used to determine the required blade stiffness of the model and is calculated, *viz*

$$\omega_{flap} = \alpha_n^2 \sqrt{\frac{E_{blade} I_{blade}}{m_{blade} R^3}} \tag{4.10}$$

where E_{blade} is the modulus of elasticity of the blade, I_{blade} is the area moment of inertia of the blade, and α_n is a constant based on the harmonic excitation mode. For the first harmonic excitation mode α_n = 1.875. The blade mass, blade radius, and angular rotor speed are all known so the only unknown when calculating the non-dimensional flapping frequency is the blade stiffness, $(EI)_{blade}$. The necessary blade stiffness for the model is calculated by setting the non-dimensional flapping frequency of the model equal to that of the full-scale turbine, viz

$$(EI)_{blade,m} = \frac{\Omega_m^2 m_{blade,m}}{\Omega_p^2 m_{blade,p}} \eta^3 (EI)_{blade,p} \tag{4.11}$$

The blade stiffness actually varies along the span of the blade, so an average value was used for the calculations herein.

It was previously assumed that the slope of the blade lift curve remains constant and that the blade chord scales with the blade radius, so these assumptions must be held true when designing the model blade to have the proper stiffness.

4.3 Scaling Results

The full-scale wind turbine is based on a turbine that uses the Sandia 100 m glass blade[28] that has a mass of 55.9 Mg and an average blade stiffness of approximately 50×10^9 N•m^2. The chord length of the blade varies across the span, but the average chord length is approximately 5 m. The other required properties of the full-scale turbine can be found in Table 4.1.

The fluid-structure dynamics of the wind turbine may be tested in the NASA Ames wind tunnel as well as a water channel at the University of Virginia. For the NASA Ames wind tunnel test, the blade radius is scaled down from 100 m to 0.5 m. For the water channel test, the blade radius is scaled down from 100 m to 0.15 m. For both tests, the tip-speed ratio, Lock number, Froude number, and non-dimensional flapping frequency were all held constant to accurately capture the fluid dynamics. The scaling results for both the wind tunnel and water channel tests compared to the full-scale are shown in Table 4.1.

The model blade mass is cubically dependent on the length scaling factor, which leads to an extremely light blade for the wind tunnel case. The water tunnel case actually has a smaller length scaling factor, but the increased density of the water helps to increase the required blade mass. The model flow speeds are approximately one order of magnitude smaller than the full-scale flow speed. The water channel flow speed may vary, depending on the density of the blade that is used. If the density of the blade is large enough that the ratio of the density of the fluid to the density of the blade is negligible, the flow speed would increase to 0.484 m/s. If the density of the blade is only twice the density of water, the flow speed would decrease to 0.342 m/s.

The required blade stiffness of the full- and model-scales differ by approximately twelve orders of magnitude. Initially, this difference is surprising, but upon closer inspection this disparity should be expected. The area moment of inertia of the blade (I_{blade}) is proportional to the characteristic length to the fourth power. The difference in the length scales is nearly three orders of magnitude, so the dependence on the length scale to the fourth power accounts for nearly all of the twelve orders of magnitude difference.

The velocity and size constraints of the wind tunnel and water channel prevent the Reynolds number and Mach number of the model-scale to be matched with the full-scale. For both cases,

the Reynolds number is off by approximately three orders of magnitude. Despite having a smaller length scale and lower flow speed, the water channel case has a larger Reynolds number than the wind tunnel case, due to the higher density of the water as compared to air. Even though the Mach number is not matched between the model- and full-scales, the Mach number is small enough for all cases that the flow can be assumed to be incompressible, so the variation in the Mach number will have a negligible impact on the flow.

4.4 Conclusions

Scaled models of a wind turbine system may be tested in both the NASA Ames wind tunnel and a water channel located at the University of Virginia. To accurately model the system dynamics, several parameters must be kept constant between the full-scale and model-scales: the tip-speed ratio, Reynolds number, Mach number, Lock number, Froude number, and non-dimensional flapping frequency. Constraints on the flow speed and model size prevented the Reynolds number and Mach number from being matched, but the tip-speed ratio, Lock number, Froude number, and non-dimensional flapping frequency were all held constant. The required blade mass for the experiments was calculated by keeping the Lock number constant and the required flow velocity was calculated by keeping the Froude number constant. The tip speed ratio was used to calculate the rotor speed based on the flow speed. Finally, the non-dimensional flapping frequency was used to calculate the required blade stiffness. The difference in the Mach numbers between the full- and model-scales will not impact the test results, because the Mach number is small enough for all cases that the flow is considered incompressible flow, but the difference in the Reynolds number will have an impact on the flow dynamics.

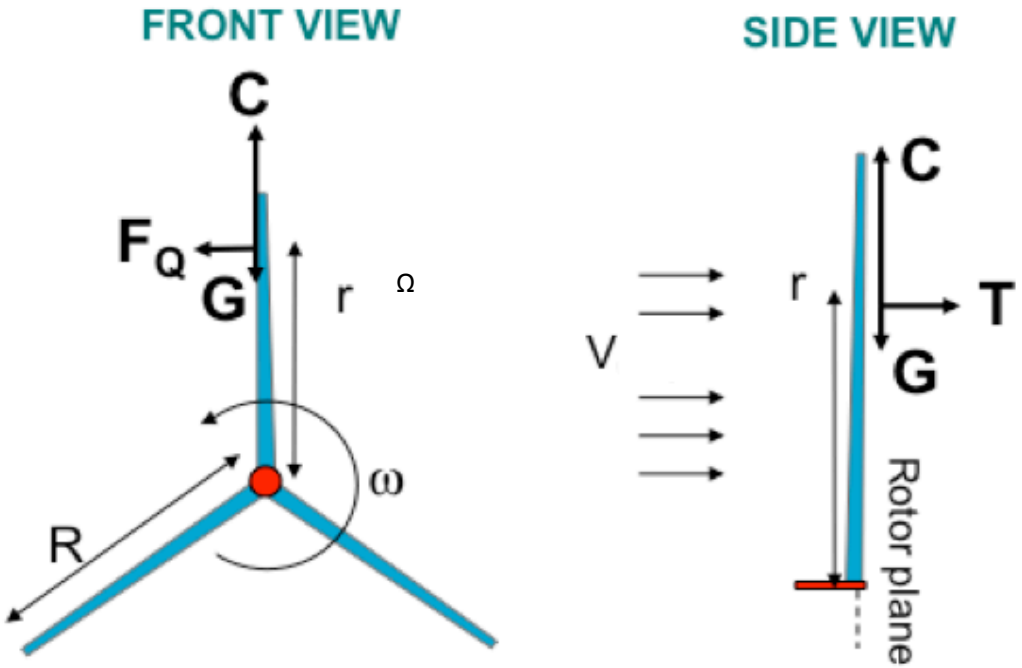

Figure 4.1: Forces on a horizontal wind turbine blade.

Table 4.1: Dynamic Scaling Results

Aspect	Full-Scale	Wind Tunnel Scale	Water Channel Scale
Rotor Radius (R)	100 m	0.5 m	0.15 m
Length Scaling Factor (η)	1	0.005	0.0015
Lock Number (Lo)	47.0	47.0	47.0
Froude Number (Fr)	0.159	0.159	0.159
Tip-Speed Ratio (λ)	8	8	8
Flapping Frequency (ϖ_{flap})	3.32	3.32	3.32
Blade Mass (m_{blade})	55.9 Mg	6.99 g	0.159 kg
Flow Speed (V)	12.5 m/s	0.884 m/s	0.453 m/s
Rotor Speed (Ω)	1 Hz	14.1 Hz	24.2 Hz
Blade Stiffness ($(EI)_{blade}$)	50×10^{9} N•m^2	11.0×10^{-3} N•m^2	11.6×10^{-3} N•m^2
Reynolds Number (Re)	4.17×10^{6}	1.47×10^{3}	3.40×10^{3}
Mach Number (M)	36.4×10^{-3}	2.58×10^{-3}	0.302×10^{-3}

Chapter 5

Summary

This study is the first to design an aerodynamic fairing specifically for use on a wind turbine tower. The fairing helps to reduce the effects that the wake of a wind turbine tower has on the blades of a downwind turbine. The aerodynamic fairing was designed to meet four requirements: 1) low drag, 2) a short trailing edge relative to the tower center, 3) a moment that results in self-alignment about the cylinder center, and 4) no large adverse pressure gradients. Several aerodynamic designs were developed and investigated using XFOIL to describe the aerodynamic performance.

The computational results showed that symmetric NACA airfoils had a lower drag than elliptical airfoils, and a three-to-one chord-to-thickness ratio results in the minimum drag for a fixed thickness, so the baseline design was chosen to be a NACA0033 airfoil. Unfortunately, the pitching moment of the NACA0033 at non-zero angles of attack would result in the fairing further misaligning with the wind direction when the tower is located at the maximum thickness.

Six new airfoils were created and analyzed along with two Eppler strut airfoils and the baseline NACA0033. The Eppler strut airfoils performed well in terms of drag and pitching moment, but they have an aggressive pressure distribution that may lead to flow separation. Of the other airfoils considered, the C30u consistently displayed the best performance with respect to drag and pitching moment. With no easy and accurate way to computationally predict flow

separation at high Reynolds numbers, a series of experiments were conducted in a water channel to determine which design is truly the best.

Flow visualization and PIV were used to analyze flow separation and wake effects of E863 and C30u airfoil models at 0°, 10°, and 20°. The flow visualization results showed that at 0°, the flow remained attached, but at 10° and 20°, the flow separated almost immediately for both airfoils. The Reynolds number for the experiments was two orders of magnitude less than the full-scale Reynolds number, so the flow is more likely to remain attached for the full-scale fairing. The dye experiments showed no discernable differences between the two airfoils with respect to flow separation at the lower Reynolds number.

From the PIV results it appeared that there were few differences between the performances of the C30u and E863 airfoils, although the C30u performed slightly better at lower angles of attack, and the E863 performed slightly better at higher angles of attack. The wake effects of the C30u and E863 airfoils were significantly lower than the cylinder wake effects at 0°. At 10°, the airfoils performed slightly better than the cylinder, but the advantages of the tower shroud are not as pronounced at this angle of attack as they are at 0°, and the cylinder actually appeared to have a better performance than the airfoils at 20°. One likely factor for the reduced performance of the airfoils compared to the cylinder at higher angles of attack is that flow separation occurs at the experimental Reynolds number. At the full-scale Reynolds number, the flow around the airfoils is more likely to remain attached, which would result in improved performance.

From the computational and experimental analyses, both the C30u and E863 are good candidates for the fairing geometry, but without running experiments closer to the full-scale Reynolds number, it is difficult to determine the best design. Future work should focus on

developing experiments that can determine the performance of the airfoils at high Reynolds numbers.

When a final design is chosen for the tower fairing, the next step is to run experiments using scaled models of the full wind turbine system. To accurately predict the performance of the wind turbine, the flow dynamics of the system must be scaled properly. To achieve the proper dynamic scaling, several parameters must be kept constant between the full-scale and model-scales: the tip-speed ratio, Reynolds number, Mach number, Lock number, Froude number, and non-dimensional flapping frequency.

An analysis was performed to determine the required conditions to achieve dynamically scaled models for use in the NASA Ames wind tunnel and a water channel at the University of Virginia. Constraints on the flow speed and model size prevented the Reynolds number and Mach number from being matched. The difference in the Mach numbers between the full- and model-scales will not impact the test results, because the Mach number is small enough for all cases that the flow is considered to be incompressible, but the difference in the Reynolds number will have an impact on the flow dynamics. The tip-speed ratio, Lock number, Froude number, and non-dimensional flapping frequency were all held constant, and from these parameters, the required blade mass, flow velocity, rotor speed, and blade stiffness were calculated.

References

[1] Loth, E., Selig, M.S., and Moriarty, P., “Morphing Segmented Wind Turbine Concept," *AIAA Applied Aerodynamics Conference*, AIAA-2010-4400, Chicago, IL, June 2010.

[2] Loth, E., Steele, A., Ichter, B., Selig, M.S., and Moriarty, P., “Segmented Ultralight Pre-Aligned Rotor for Extreme-Scale Wind Turbines,” *AIAA Aerospace Sciences Meeting*, AIAA-2012-1290, Nashville, TN, Jan. 2012.

[3] Ichter, B., Steele, A., Loth, E., and Moriarty, P., “Structural Design and Analysis of a Segmented Ultralight Morphing Rotor (SUMR) for Extreme-Scale Wind Turbines,” *AIAA Fluid Dynamics Conference*, AIAA-2012-3270, New Orleans, LA, June 2012.

[4] Hand, M., Simms, D., Fingersh, L.J., et al., “Unsteady Aerodynamics Experiment Phase VI: Wind Tunnel Test Configurations and Available Data Campaigns,” NREL/TP-500-29955, Dec. 2001.

[5] Rasmussen, F., Petersen, J.T., Volund, P. Leconte, P, Szechenyi, E and Westergaard, C. “Soft Rotor Design for Flexible Turbines“, Riso National Laboratory, Roskilde, Denmark, Contract JOU3-CT95-0062.

[6] Zahle, F., Sørensen, N.N., and Johansen, J., "Wind Turbine Rotor-Tower Interaction Using an Incompressible Overset Grid Method," *Wind Energy*, Vol. 12, No. 6, Sep. 2009, pp. 594-619.

[7] Baker, J.P., Standish, K.J., and van Dam, C.P., "Two-Dimensional Wind Tunnel and Computational Investigation of a Microtab Modified Airfoil," *Journal of Aircraft*, Vol. 44, No.2, 2007, pp. 563-572.

[8] Cooperman, A.M., Chow, R., and van Dam, C.P., "Active Load Control of a Wind Turbine Airfoil Using Microtabs," *Journal of Aircraft*, Vol. 50, No. 4, 2013, pp. 1150-1158.

[9] Lee, S.J., Lee, S.I., and Park, C.W., "Reducing the Drag on a Circular Cylinder by Upstream Installation of a Small Control Rod," *Fluid Dynamics Research*, Vol. 34, No. 4, Apr. 2004, pp. 233-250.

[10] Mashud, M., Islam, M.S., Bari, G.S., and Islam, M.R., "Reduction of Drag Force for a Cylinder by Attaching Cylindrical Rings," *Asian Congress of Fluid Mechanics*, Dhaka, Bangladesh, Dec. 2010, pp. 174-177.

[11] Sosa, R., D'Adamo, J., and Artana, G., "Circular Cylinder Drag Reduction by Three-Electrode Plasma Actuators," *Journal of Physics: Conference Series*, Vol. 166, No. 1, 2009.

[12] Hwang, J.Y., Yang, K.S., "Drag Reduction on a Circular Cylinder Using Dual Detached Splitter Plates," *Journal of Wind Engineering and Industrial Aerodynamics*, Vol. 95, No. 7, July 2007, pp. 551-564.

[13] Triyogi, Y., Suprayogi, D., and Spirda, E., "Reducing the Drag on a Circular Cylinder by Upstream Installation of an I-type Bluff Body as Passive Control," *Journal of Mechanical Engineering Science*, Vol. 223, Oct. 2009, pp. 2291-2296.

[14] Eppler, R., *Airfoil Design and Data*, Springer-Verlag Berlin Heidelberg, 1990.

[15] Janajreh, I., Talab, I., and Macpherson, J., "Numerical Simulation of Tower Rotor Interaction for Downwind Wind Turbine," *Modelling and Simulation in Engineering*, 2010.

[16] Jonkman, J., Butterfield, S., Musial, W., and Scott, G., "Definition of a 5-MW Reference Wind Turbine for Offshore System Development", NREL/TP-500-38060, February 2009.

[17] Drela, M., "XFOIL: An Analysis and Design System for Low Reynolds Number Airfoils," *Conference on Low Reynolds Number Airfoil Aerodynamics*, University of Notre Dame, June 1989.

[18] Abbott, I. and von Doenhoff, A., *Theory of Wing Sections: Including a Summary of Airfoil Data*, New York: Dover Publications, 1959.

[19] Blevins, R., *Applied Fluid Dynamics Handbook*, Van Nostrand Reinhold Company Inc., New York, 1984.

[20] Selig, M.S. and Maughmer, M.D., "Generalized Multipoint Inverse Airfoil Design," *AIAA Journal*, Vol. 30, No.11, Nov. 1992, pp. 2618-2625.

[21] Merzkirch, W., "Techniques of Flow Visualization," AGARD Report, Dec. 1987.

[22] Werlé, H., "Hydrodynamic Flow Visualization," *Annual Review of Fluid Mechanics,* Vol. 5, Jan. 1973, pp. 361-382.

[23] Erickson, G.E., "Water Tunnel Flow Visualization: Insight into Complex Three-Dimensional Flowfields," *Journal of Aircraft,* Vol. 17, No. 9, 1980, pp. 656-662.

[24] *Wind Turbines – Part 1: Design Requirements,* IEC 61400-1, Third Edition, Aug. 2005.

[25] Selig, M.S. and McGranahan, B.D., "Wind Tunnel Aerodynamic Tests of Six Airfoils for Use on Small Wind Turbines," National Renewable Energy Laboratory, NREL/SR-500-34515, Oct. 2004.

[26] Uzol, O. and Camci, C., "The Effect of Sample Size, Turbulence Intensity and the Velocity Field on the Experimental Accuracy of Ensemble Averaged PIV Measurements," *4th International Symposium on Particle Image Velocimetry*, Sep. 2001.

[27] Bottasso, C., Campagnolo, F., Croce, A., Maffenini, L., "Development of a Wind Tunnel Model for Supporting Research on Aero-servo-elasticity and Control of Wind Turbines", *13th International Conference on Wind Engineering*, Amsterdam, The Netherlands, ICWE13, July 2011.

[28] Griffith, T. and Ashwill, T., *The Sandia 100-meter All-glass Baseline Wind Turbine Blade: SNL100-00,* Albuquerque, NM: Sandia National Laboratories, SAND2011-3779, 2011.